https://doi.org/10.5194/egusphere-2026-2104
Preprint. Discussion started: 8 May 2026

Dual frequency airborne SAR experiment on snow water equivalent retrieval in Alpine terrain

Helmut Rott[1], Thomas Nagler[1], Markus Hetzenecker[1], Ralf Horn[2], Jens Fischer[2], Julia Kubanek[3]

[1]ENVEO IT GmbH, A 6020 Innsbruck, Austria
[2]Microwaves and Radar Institute, German Aerospace Center (DLR), D 82234 Wessling, Germany
[3]ESA ESTEC, NL 2200 Noordwijk, The Netherlands

Correspondence to: Helmut Rott (helmut.rott@enveo.at)

Abstract. In March 2021 a field experiment was conducted in the high-Alpine test site Woergetal of the Austrian Alps, exploring the feasibility and performance of snow water equivalent (SWE) and snow depth retrievals by means of C- and L-band SAR data. Multiple repeat-pass acquisitions were acquired along two flight tracks with an airborne SAR system. The SAR acquisitions spanned two snowfall events of different intensity. In situ data on physical snow properties were collected throughout the campaign. Main objective was the development and evaluation of procedures for SWE monitoring by measuring the interferometric path delay in snow, with focus on the future Radar Observation System for Europe at L-band (ROSE-L), the Sentinel-1 Next Generation mission, and the proposed geosynchronous C-band SAR mission Hydroterra. The response of the VH/VV backscatter ratio and the co-polarized phase differences (CPD) to snow accumulation was also studied. These two parameters do not show a reproducible relation with snow depth and SWE of the snowfall events. CPD measured after snowfall shows an increase with the incidence angle that can be attributed to radar wave propagation through a refrozen crust formed before the snowfall. For the interferometric SWE retrievals three input data configurations were applied: (1) C- and L-band repeat-pass SAR data at full spatial resolution; (2) differential wavenumber (Delta-k) interferograms obtained by split-bandwidth processing; (3) simulated geosynchronous C-band SAR data reflecting the properties of the Hydroterra mission. Coherence, interferometric phase and computed snow accumulation (ΔSWE) images and their properties are documented for these configurations. L-band case 1 shows high coherence and good retrieval performance for both snowfall events. C-band case 1 and case 3 show high coherence and good performance for the low intensity snowfall but low coherence and 2π phase ambiguity prohibit the application for the intense snowfall. This deficiency can be overcome by the Delta-k approach which delivers suitable results for both frequencies. Options for complementary use of the different approaches are discussed.

https://doi.org/10.5194/egusphere-2026-2104
Preprint. Discussion started: 8 May 2026

1 Introduction

The lack of regular, spatially detailed area-wide observations snow mass (snow water equivalent, SWE) and snow depth is a main gap in global cryosphere monitoring (Mortimer et al., 2020). Spaceborne synthetic aperture radar (SAR) systems offer various options for resolving this deficiency, as these sensors provide high spatial resolution and microwave signals at centimetre wavelength are able to penetrate snow as long as it is dry. Various approaches have been tested and applied for snow depth and SWE retrievals by means of imaging radar systems. The use of these techniques for wide-spread satellite-based operational monitoring applications is still pending. The approaches for snow depth and SWE retrievals addressed below refer to dry snow because the dielectric losses in wet snow are high resulting in very limited penetration depth.

Comprehensive studies and experiments on the inversion of radar backscatter intensity in terms of snow depth and SWE have been performed, with focus on short radar wavelength (Rott at al. 2010; Zhu et al. 2018). Theory and experimental studies confirm the high potential of Ku-and X-band radar sensors for SWE monitoring (Tsang et al., 2022). However, the backscatter signal depends also on snow microstructure, snow density and stratification, prior estimates of which are needed for retrieving SWE and snow depth (Pan et al., 2024; Singh et al., 2024). Tower-based polarimetric backscatter measurements over an alpine snowpack show also that also in C-band changes in microstructure, stratigraphy, melt–freeze metamorphism have a major impact on the backscatter signal, affecting possible relations between backscatter intensity and snow depth (Brangers et al., 2024).

A promising method for mapping SWE at high spatial resolution is differential radar interferometry (DInSAR), exploiting the path delay of a radar signal propagating through a snow layer (Guneriussen et al., 2001). The radar should operate in a wavelength for which the absorption and scattering losses in snow are small so that the main backscatter contribution comes from the snow/ground interface. For dry seasonal snow this is the case for C-band and lower radar frequencies. At these frequencies the DInSAR approach for SWE retrieval is only marginally affected by snow microstructure as long as the snow is dry. Critical issues for DInSAR SWE retrievals are temporal decorrelation of the interferometric signal and the 2π phase ambiguity.

The validity of the interferometric approach has been well demonstrated with ground-based and spaceborne radar systems. Leinss et al. (2015) derived time series of snow accumulation in Sodankylä, Finland, for four winter seasons from sequences of interferometric data measured in the 10 GHz to 16 GHz frequency range with a ground based scatterometer. The impact of temporal decorrelation was minimized by means of repeat observations in 4 h time steps. Early case studies over the Alps and Alaska, using C-band SAR images of the ERS-1 satellite acquired during the 3-day repeat pass orbit ice phase, demonstrated the InSAR sensitivity in respect to SWE (Rott et al., 2004; Deeb et al., 2011). Recent studies focus on the use of L-band SAR for SWE retrievals, preparing for snow monitoring applications of the NASA–ISRO (NASA–Indian Space Research Organization) SAR (NISAR) mission launched in July 2025 (Tarricone et al., 2023; Bonnell et al., 2024; Hoppinen et al., 2024A).

https://doi.org/10.5194/egusphere-2026-2104
Preprint. Discussion started: 8 May 2026

Here, we report on a field campaign performed in the Austrian Alps that addresses the feasibility and performance of SAR-based techniques for SWE and snow depth observations in mountainous terrain. Main motivation for the field experiment was the evaluation of the InSAR-based SWE measurement approach in preparation of snow monitoring applications for the upcoming polar-orbiting SAR missions ROSE-L (Radar Observation System for Europe at L-band) (Iannini et al., 2024), the Sentinel-1 NG (Next Generation) C-band SAR mission of the European Copernicus Programme and the Hydroterra mission. Hydroterra was proposed to ESA in response to the Call for Earth Explorer 10 Mission Ideas, consisting of a single satellite with a C-band SAR operating in a geosynchronous orbit (ESA, 2020). An updated version for a geosynchronous C-band SAR mission, called Hydroterra+, was proposed to ESA in 2023 in response to the Call for Earth Explorer 12 Mission Ideas. Feasibility studies for the Hydroterra+ mission are currently going on in the context of preparations for Earth Explorer 12 mission candidates.

During the field experiment, performed in March 2021, C- and L-band polarimetric repeat-pass SAR data were acquired with the airborne F-SAR system on several days, spanning two snowfall events of different intensity. Main objective was the testing and evaluation of SWE retrievals based on the inversion of repeat-pass interferometric SAR data. Additionally, the portfolio of dual frequency complex SAR data and coincident in situ snow measurements was used for checking the response of the SAR backscatter intensity and the co-polarized phase difference in respect to the accumulation of fresh snow. Section 2 provides an overview on the study area, on field measurements and on the acquired airborne SAR data. Section 3 deals with the response of the co- and cross-polarized backscatter intensity and the co-polarized phase-difference to the accumulation of fresh snow. Section 4 describes the procedures used for deriving the amount of fresh snow (ΔSWE) from interferometric SAR data, shows coherence and ΔSWE products and presents a performance analysis. Input data in three different configurations are used for ΔSWE retrievals: (1) full resolution F-SAR data, (2) Delta-k interferometric data, derived from full resolution F-SAR data by means of split-bandwidth processing, (3) simulated geosynchronous SAR data. In Section 5 specific features of the different approaches are discussed and their particular capabilities and constraints are set forth.

2 Study area and data

The in situ snow measurements and the analysis of airborne SAR data focus at locations above the treeline in Wörgetal, a secondary valley draining into Nederbach and Ötztaler Ache, a tributary to the river Inn. Wörgetal is located in the Stubaier Alpen, 35 km west of Innsbruck, Austria.

2.1 Description of the study area

Figure 1 shows an aerial photo image map of Wörgetal (Orthofotos-Tirol, 2020) with locations of snow measurements, corner reflectors and heading of the flight tracks. The heading of track 10 is exactly north-south and of track 11 exactly south-north. The area of Wörgetal, outlined in Fig.1, extends from 2000 m to 2720 m in elevation and has steep slopes on the eastern,

https://doi.org/10.5194/egusphere-2026-2104
Preprint. Discussion started: 8 May 2026

southern and western sections of the valley. Transects of snow depth and density measurements are located in sections with moderate topography. Also the analysis of radar signatures and the SWE retrievals were performed in sections with gentle terrain (regions of interest, RoIs) that exclude zones with steep fore-slopes and layover in any of the two tracks. This facilitates comparisons between the two tracks and enables the consistent assessment of uncertainties, reducing impacts of noise arising from uncertainties of topographic correction in steep terrain. Mean elevations and radar incidence angles of the three RoIs (OB - Oberer Boden, MB – Mittlerer Boden, UB – Unterer Boden) are specified in Table 1. Supplement Fig. S1 shows a view along Wörgetal. In geocoded SAR images (Fig. S2) the impact of terrain-induced radiometric noise on steep fore-slopes is evident, affecting east-facing slopes in track 10 and west-facing slopes in track 11.

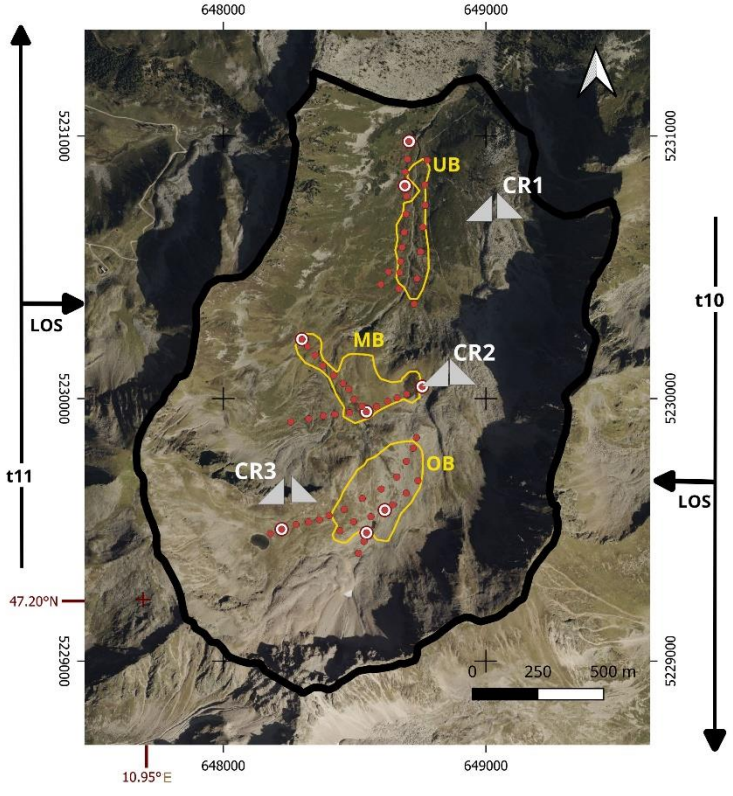

Figure 1: Aerial photo image map of Wörgetal. The numbers along the frame are coordinates of the UTM zone 32 N, easting and northing. CR corner reflectors; • • • • transect of snow depth measurements; ⊙ snow pits; OB, MB, UB – outlines of main sites (RoIs) for radar signature analysis and SWE retrievals; t10, t11 heading of F-SAR flight tracks; LOS - radar line-of-sight.

The surface characteristics of the subnivean ground vary between the three RoIs, showing differences in surface roughness and decreasing density of vegetation with elevation. The UB surface cover is dominated by dwarf shrubs, in particular Alpine rhododendron and vaccinium, and includes a few plots covered by scree. MB has the smoothest surface of the three RoIs. The area is almost completely covered by sedges and grasses and includes some marshy sections. About 70 % of OB are bare

https://doi.org/10.5194/egusphere-2026-2104
Preprint. Discussion started: 8 May 2026

surfaces covered by debris of different size. Some parts are covered by sparse Alpine grassland. At the time of the campaign the vegetation was dormant and the soil unfrozen, common features for subnivean surfaces at the given elevation throughout winter.

Topographic features and surface roughness are highlighted in Fig. S3, showing a shaded DEM of Wörgetal with 0.5 m x 0.5 m spatial resolution, based on airborne lidar data. Roughness features at different spatial scales are evident. In order to check the relevance of roughness for backscatter intensity and coherence we computed the standard deviation of the surface height of the 0.5 m x 0.5 m pixels within cells of 5 m x 5 m spatial extent, representing small- to medium-scale surface roughness. The mean values of the standard deviation of all cells within an RoI are: OB: 0.305 m, MB: 0.217 m, UB: 0.398 m. The surface of MB is smoother than at the two other sites which is also evident in Fig. S3.

Table 1. RoI elevation, mean radar look angle (θ_L) and mean value and standard deviation of the incidence angle (θ_i) for F-SAR images of track 10 and track 11.

RoI	Mean elevation [m] a.s.l.	θ_L track 10	θ_i mean track 10	θ_i track 10 std. dev	θ_L track 11	θ_i mean track 11	θ_i track11 std. dev
OB	2335	25.8	28.3	8.2	33.4	37.4	6.0
MB	2250	28.7	31.8	5.9	33.8	33.6	5.4
UB	2095	29.5	32.8	7.2	38.4	32.1	9.0

2.2 In situ data on snow properties and their temporal evolution

Eight F-SAR measurement flights were performed over Wörgetal between 2 and 19 Mach 2021. The flights spanned two snow fall events of different intensity. Figure 2 shows the air temperature record from 1 March to 25 March 2021 at the station Gossenkölle, located 4.5 km north-east of Wörgetal OB at an elevation of 2427 m. The snow depth (SD) is based on in situ measurements at OB, using the temporal evolution of the snow depth record at Gossenkölle for estimating the temporal sequence.

In preparation of the campaign six corner reflectors (three east-facing, three west-facing) were mounted on solid, snow-free ground. On each day with flights the corner reflectors were cleaned out of snow before the first flight. Field measurements of snow depth and physical snow properties were performed on 2, 3, 6, 9, 13 and 19 March 2021. The snow depth was measured along transects in steps of about 50 m distance, stretching across the RoIs and also on parts of the surrounding areas. The snow depth point values used for comparison and validation are mean values of several probings within 3 m x 3 m plots. The measurements on 2 and 3 March covered snow depth and physical properties of the total snowpack. The measurements on the days after the snowfall events (6 March, 19 March) focused on the depth, density and morphology of the fresh snow.

https://doi.org/10.5194/egusphere-2026-2104
Preprint. Discussion started: 8 May 2026

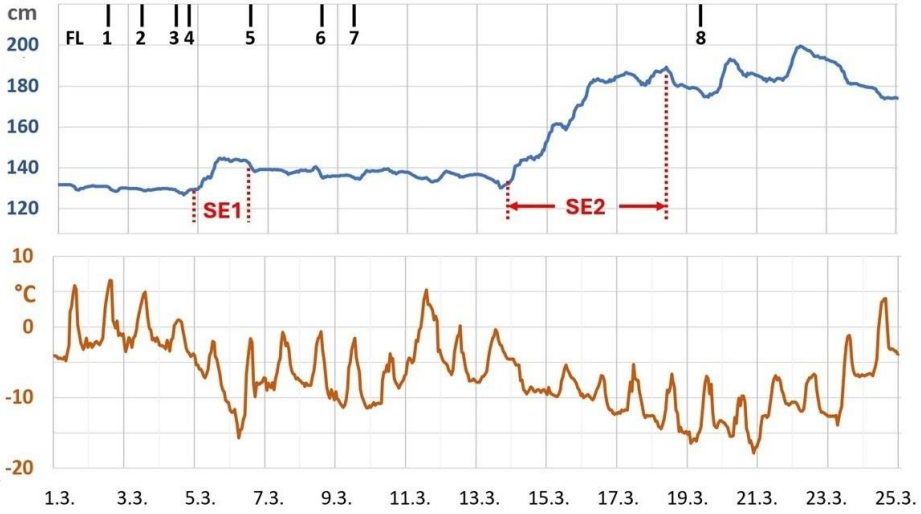

Figure 2: Air temperature (°C) record at the station Gossenkölle and snow depth (cm) at Wörgetal OB, 1 March to 25 March 2021. SE1 and SE2: snowfall events spanned by repeat-pass InSAR data. FL1 to FL8: F-SAR flights.

The 2020/2021 snow cover season started in October 2020 with several days of snowfall down to about 1500 m elevation. The snow cover melted largely away in early November, but on high elevation sites with low exposure to solar illumination the October snow persisted throughout winter. This was the case in some sections of OB where a crust of melt-freeze polycrystals formed that persisted throughout winter as evident in the snow pit profile (Fig. S4A). Major snowfall events took place in December and January. On 22 December 2020 a passing warm front caused rain up to about 2300 m elevation. This is reflected in a frozen crust between 53 cm and 59 cm snow height at MB and UB (Fig. S4B). The grain shape of the main snow layers was dominated by solid faceted crystals, tracing back to temperature gradient metamorphism.

February 2021 was sunny and dry, and the mean air temperatures were above the long-term average. The snow measurements at the time of the F-SAR flights in the morning of 2 and 3 March showed at MB and UB a frozen surface crust of 2 cm thickness (Fig. S4B). The average total snow depth measured along transects on 2 and 3 March amounted at OB to 141 cm, at MB to 128 cm, and at UB to 116 cm (Table 2). The related SWE values, listed in Table 2, are based on these SD numbers, multiplied by the average snow density measured in snow pits: OB $\langle\rho\rangle$ = 347.7 kg m^{-3}, MB $\langle\rho\rangle$= 326.6 kg m^{-3}, UB $\langle\rho\rangle$ = 350.8 kg m^{-3}. The first snowfall event (SE1), spanned by F-SAR repeat-pass acquisitions, took place on 5 March 2021. The F-SAR flights and in situ measurements were performed in the morning of 6 March. The fresh snow had not been affected by wind. The crystals were of six-fold stellar shape. The average depth of the fresh snow at the RoIs amounted to 13.7 cm (Table 2), the average density of the fresh snow was 95 kg m^{-3}. The snow at the RoIs was not affected by surface melt, but on steep east- and south-facing slopes a thin surface melt layer formed around noon.

https://doi.org/10.5194/egusphere-2026-2104
Preprint. Discussion started: 8 May 2026

Table 2. RoI mean values and standard deviation of total snow depth and SWE measured on 2 and 3 March 2021. Depth of fresh snow (ΔSD) and ΔSWE measured on 6 March (after snowfall event SE1) and on 19 March (after snowfall event SE2).

RoI	Total SD [cm] 2&3 March	Total SD std. dev.	Total SWE [mm]	ΔSD SE1 [cm]	ΔSD SE1 std. dev.	SE1 ΔSWE [mm]	ΔSD SE2 [cm]	ΔSD SE2 std. dev.	SE2 ΔSWE [mm]
OB	140.8	29.4	486.7	15.6	2.1	14.8	43.2	2.3	62.6
MB	127.6	41.2	416.7	13.3	2.4	12.6	45.5	6.2	66.0
UB	116.2	37.8	407.6	12.3	1.1	11.7	42.1	6.1	61.0

The tightest F-SAR repeat acquisition period spanning the second snowfall event (SE2) extends from 9 to 19 March 2021. SE2 covers several occurrences of snowfall from 14 to 18 March. During the field measurements on 19 March the temperature of the total snowpack was below -5°C. The F-SAR repeat time span includes in the beginning three days with full solar irradiance and maximum air temperatures near or above 0°C. The highest temperature was observed on 11 March, causing wetting of the snow surface up to 3000 m elevation on sun-exposed slopes and up to 2400 m on north slopes (Lawinenwarndienst Tirol, 2021). A frozen melt crust (6 cm thickness at OB) formed before the subsequent snowfall event when the temperature was consistently below -5°C. The fresh snow accumulating on top of the crust was partly subject to wind-induced decomposition and settlement. This resulted in a critical avalanche hazard situation with many avalanche releases on several days as from 17 March 2021 (Lawinen Report, 2021).

The average depths of snow (ΔSD), deposited during SE2 on the refrozen crust and measured in the morning of 19 March, amounted to 43.2 cm, 45.5 cm and 42.1 cm in OB, MB and UB (Table 2). The mean density was 145 kg m^{-3}, resulting in mean ΔSWE values of 62.6 mm, 66.0 mm and 61.0 mm. The spatial variability of ΔSD did not show a consistent trend with altitude. Spatial variations of ΔSD within the RoIs were primarily determined by small-scale topography.

2.3 Airborne SAR measurements

The airborne SAR measurements over Wörgetal were performed with DLR's airborne radar system F-SAR installed on board a DO228 aircraft. F-SAR is a fully polarimetric and interferometric airborne radar system, which can operate in X-, C-, S-, L- and P-band (Horn et al., 2017). Over Wörgetal F-SAR operated in fully polarimetric dual-frequency, C- and L-band, mode. The SAR data were acquired along two tracks from a flight altitude of 5700 m above the WGS84 ellipsoid, resulting on the RoIs in mean incidence angles between 28.3 and 37.4 degrees (Table 1). For F-SAR SAR data processing and data analysis a Digital Elevation Model (DEM) with 5 m spatial resolution was used, based on airborne Laser scans (Orthofotos-Tirol, 2020).

Table 3 shows the SAR frequencies and signal bandwidths selected for the Wörgetal data acquisitions and the processing parameters of the full resolution data. Pre- and post-campaign calibration flights were performed over DLR's calibration site Kaufbeuren on 1 March and 24 March 2021. Additional calibration flights were performed on 3 March. The corner reflectors set up at Wörgetal provided a basis for checking the radiometric, polarimetric and interferometric calibration and for assessing

https://doi.org/10.5194/egusphere-2026-2104
Preprint. Discussion started: 8 May 2026

the geolocation accuracy of the processed data. The exact position of the corner reflectors was measured with high-precision GPS equipment. One of the three west-facing corner reflectors (CR3W) was subject to ambiguities due to reflection from a steep fore-slope, affecting the radar cross section and phase. The three east-facing reflectors were used as phase reference and for checking radiometric and polarimetric calibration of track 10 and two of the west-facing reflectors (CR1W and CR2W) were used for track 11. The leg length of the deployed corner reflectors is 0.95 m which is suitable as reference for radiometry of the C-band channel, but insufficient for radiometric calibration in L-band. All reflectors were used for both SAR channels as geodetic tie points.

Table 3. Main F-SAR sensor and processing parameters of the Wörgetal campaign data.

	C-band	L-band
Centre frequency	5300 MHz	1325 MHz
Range bandwidth	384 MHz	150 MHz
Azimuth resolution	0.50 m	0.60 m
Slant range resolution	0.50 m	1.30 m
Pixel size (azimuth x range)	0.2 m x 0.3 m	0.4 m x 0.6 m

Dates of the F-SAR measurement flights (FL) over Wörgetal are specified in Table 4. Each measurement flight comprised several repeat passes in both tracks, the number of which ranges from three passes per track within FL08 to eleven passes per track within FL01 and FL02. The data of different repeat passes within a flight were used for generating SAR images with different integration times in order to obtain simulated geosynchronous SAR images.

Table 4. Dates of F-SAR flights over Woergetal, day number in March 2021, M – morning, A – afternoon.

Flight Nr.	FL01	FL02	FL03	FL004	FL05	FL06	FL07	FL08
Date	02 M	03 M	04 M	04 A	06 A	08 A	09 M	19 M

Prior to standard SAR processing an initialization procedure was applied for preparing the DEM and other auxiliary data that are needed in subsequent processing. This procedure includes the conversion of the lidar DEM into slant range geometry and the determination of ideal tracks for SAR processing. One common optimal straight-line was defined for each track. Another critical parameter influencing the final SAR image geometry is the squint angle resulting from prevailing wind conditions during SAR data acquisition. SAR processing can compensate different wind conditions up to some degree. It is recommended selecting the Doppler centroid as close as possible to the actual squint angle because the image noise level increases the further the scene is processed from its actual squint angle. In order to minimize impacts of squint angle effects, pairs of flights with similar averaged squint angles were preferably used for interferometric analysis and SWE retrievals.

https://doi.org/10.5194/egusphere-2026-2104
Preprint. Discussion started: 8 May 2026

3 Analysis of backscatter intensity and co-polarized phase in response to snowfall events

The analysis of the complex SAR signals presented in this section focusses on the temporal evolution of backscatter intensity and phase and on relations of these parameters to accumulated fresh snow. The presented signatures refer to level and moderately inclined terrain. This helps to minimize impacts of topography-related noise which is evident on steep slopes. The backscatter intensity and co-polarized phase values presented below are based on full resolution F-SAR data in radar imaging geometry, applying a boxcar filter of 25 x 25 pixels size. This results in C-band cell size of 5 m x 7.5 m (azimuth x range) and L-band cell size of 10 m x 15 m. The resulting number of independent samples (N_L) is 150 in C-band and 192 in L-band. The standard deviation of backscatter intensity for a homogeneous distributed target with average power ⟨P⟩ is:

$$\sigma(P) = \frac{\langle P \rangle}{\sqrt{N_L}}\left(1 + \frac{1}{SNR}\right) \quad (1)$$

SNR is the signal-to-noise ratio. In the noise-free case the standard deviation for F-SAR cells of 25 x 25 pixels is in linear scale 0.0816 ⟨P⟩ for N_L =150 and 0.0722 ⟨P⟩ for N_L =192. The backscatter intensity values of individual RoIs represent mean values of at least 151 cells in L-band and at least 606 cells in C-band.

3.1 Response of co- and cross-polarized backscatter intensity

The mean incidence angles of track 10 and track 11 for OB, MB and UB are 32.8°, 32.7° and 32.5°, facilitating the comparison of backscatter intensities of the RoIs. In C-band the mean $\sigma°_{VV}$ values of OB and UB are the same (-7.8 dB), mean $\sigma°_{VV}$ of MB is -11.2 dB (Fig. 3A). These numbers are in accordance with the lower roughness of the ground surface at MB. In L-band the mean $\sigma°_{VV}$ values for OB, MB and UB are -8.9 dB, -11.8 dB and -10.9 dB (Fig.4A). The co-polarized backscatter ratios ($\sigma°_{HH}/\sigma°_{VV}$) show similar values in the three RoIs (Fig. S5), on average amounting to -0.7 dB in C-band and -2.2 dB in L-band. This behaviour is in accordance with backscatter theory, showing negative HH/VV backscatter ratios for rough surfaces and an increasing magnitude of the HH-VV difference with increasing wavelength (Ulaby and Long, 2014).

The mean $\sigma°_{VH}$ values of OB, MB and UB are in C-band -15.8 dB, -21.9 dB and -17.7 dB and in L-band -16.6 dB, -25.7 dB and -24.3 dB (Fig. S6). The drop of cross-polarized σ° from C- to L-band frequencies is a common feature of rough surface scattering. This effect is supressed at OB, the surface cover of which is dominated by debris of multi-scale size, an efficient source of depolarization resulting in high cross-polarized backscatter signals (Huang et al., 2017). The $\sigma°_{VH}/\sigma°_{VV}$ ratio shows a larger spread between individual sites than co-polarized σ°, in particular in L-band. The average $\sigma°_{VH}/\sigma°_{VV}$ values for OB, MB and UB are in C-band -7.5 dB, -11.2 dB and -9.8 dB (Fig. 4B) and in L-band -7.7 dB, -14.0 dB and-13.3 dB (Fig. 5B). The differences of the VH/VV ratio between individual sites and frequencies are primarily driven by the cross-polarized signal.

There was a weak trend of increase for the co-polarized σ° during the observation period (Figures 3A and 4A). The cross-polarized σ° values of both frequencies do not show a clear temporal trend (Fig. S6). C-band $\sigma°_{VH}$ of FL05 on 6 March, the day after snowfall SE1, shows a small peak in both tracks, with the average rise amounting to 0.32 dB in OB, 0.73 dB in MB

https://doi.org/10.5194/egusphere-2026-2104
Preprint. Discussion started: 8 May 2026

and 0.68 dB in UB. The spike is also reflected in the change of the C-band VH/VV backscatter ratio (ΔCR), amounting to 0.39 dB, 0.96 dB and 0.99 dB in the three RoIs. However, these ΔCR values do not reflect the observed depths of fresh snow amounting to 15.6 cm, 13.3 and 12.3 cm at the three sites. The spike of FL05 does not show up in L-band (Fig. S6 and Fig. 4B). The C-band ΔCR values of FL07 to FL08, spanning SE2, are smaller than those of FL04 to FL05 (SE1), in spite of the much larger snowfall, amounting to 0.28 dB, 0.48 dB and 0.55 dB for the three RoIs. In L-band the average ΔCR between FL07 and FL08 decreased by 0.26 dB. These numbers show that changes of the cross-to co-polarized backscatter ratio do not reflect the observed changes of snow depth and SWE.

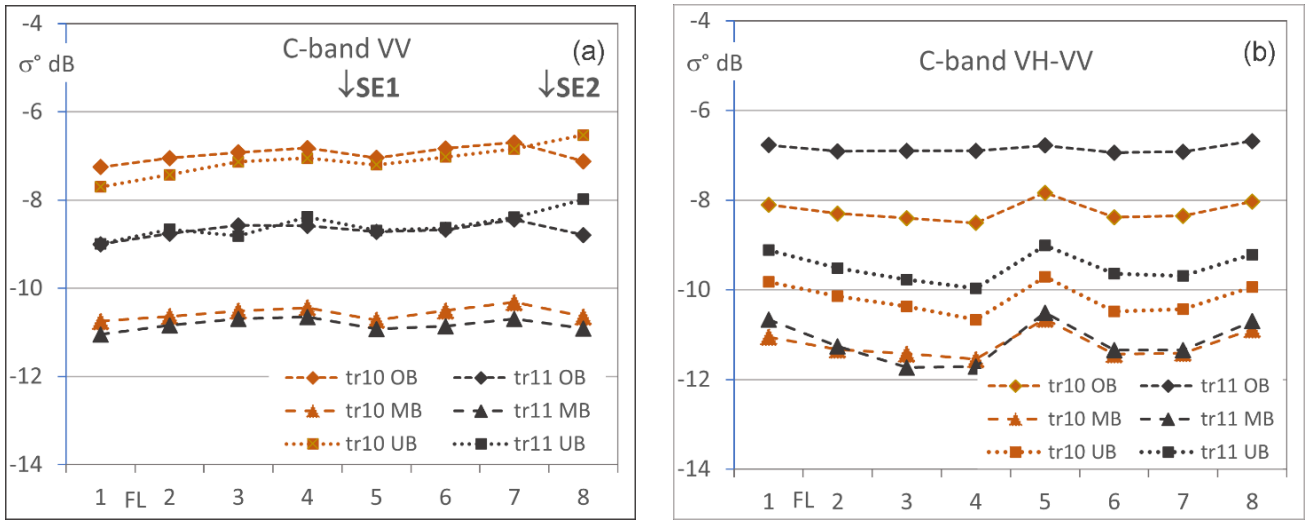

Figure 3: F-SAR C-band backscatter coefficients of the RoIs, flight 1 to flight 8, track 10 and track 11. (a) σ°_{VV}; (b) σ°_{VH}-σ°_{VV}. The arrows refer to snowfall events, SE1 between FL4 andFL5, SE2 between FL7 and FL8.

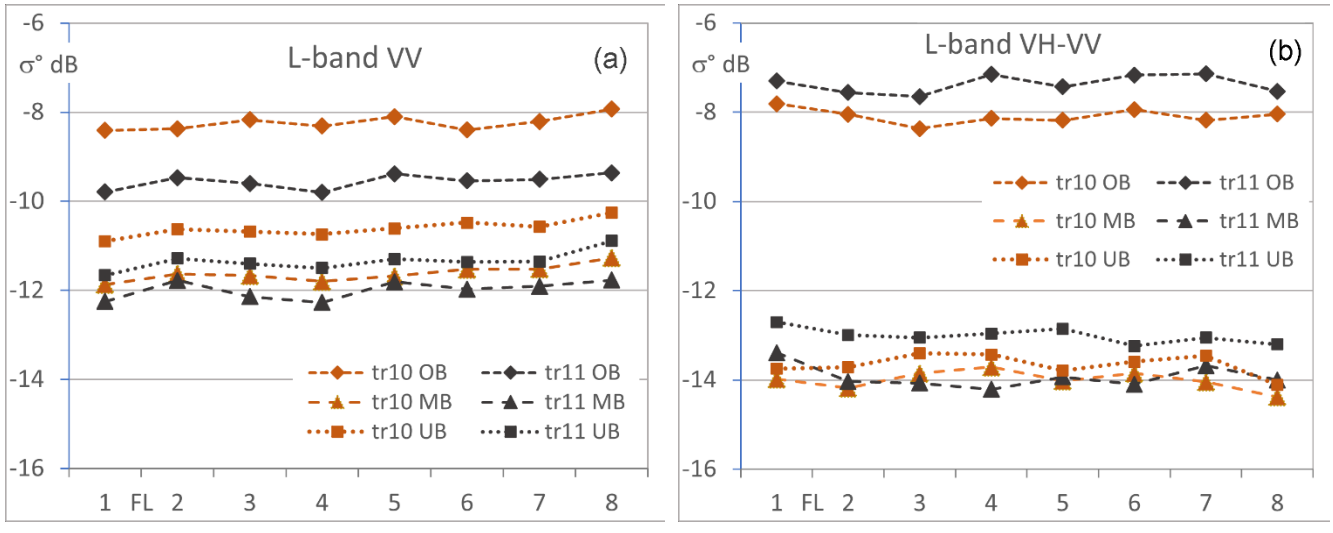

Figure 4: F-SAR L-band backscatter coefficients of the RoIs, flight 1 to flight 8, track 10 and track 11. (a) σ°_{VV}; (b) σ°_{VH}-σ°_{VV}.

https://doi.org/10.5194/egusphere-2026-2104
Preprint. Discussion started: 8 May 2026

3.2 Response of the co-polarized phase difference to fresh snow

Theoretical and ground-based polarimetric radar measurements in the 9 to 18 GHz range show distinct relations between the co-polarized phase difference (CPD) and the dielectric and structural anisotropy of seasonal snow (Leinss et al., 2016). For fresh, dry snow horizontal structures dominate, causing a change of the CPD versus the pre-snowfall state (ΔCPD). Leinss et al. (2014) show significant dependence of ΔCPD on the depth of fresh snow in time series of X-band satellite SAR data in which positive ΔCPD (VV-HH) values are related to the depth of fresh snow. On the other hand, also gravitational snow settling and densification can create horizontal structures (Leinss et al., 2020) whereas temperature gradient metamorphism gives rise to vertical structures (Calonne et al., 2014).

The CPD is the phase of the complex co-polarized correlation coefficient (coherence):

$$\gamma_{vvhh} = \frac{\langle S_{vv} \cdot S_{hh}^{*} \rangle}{\sqrt{\langle |S_{vv}|^2 \rangle \cdot \langle |S_{hh}|^2 \rangle}} \quad (2)/$$

S_{vv} and S_{hh} are single look complex backscatter data in VV and HH polarized channels. * denotes the complex conjugate and $\langle \cdot \rangle$ is the expectation value for which an estimate can be obtained by averaging over surrounding pixels. The phase angle between the two co-polarized channels is

$$\phi_{CPD} = \phi_{vv} - \phi_{hh} = arg(\gamma_{vvhh}) \quad (3)$$

The coherence magnitude, $|\gamma_{vvhh}|$ indicates the strength of correlation between VV and HH measurements. The random phase error, $\sigma_{\Phi,ran}$, of a pixel comprising N_L independent resolution elements can be estimated in dependence of coherence magnitude (Rosen et al., 2000):

$$\sigma_{\phi,ran} = \frac{1}{\sqrt{2N_L}} \frac{\sqrt{1-|\gamma|^2}}{|\gamma|} \quad [rad] \quad (4)$$

We use estimation windows (cells) of 25 x 25 pixels for computing the complex coherence, yielding N_L = 150 in C-band and N_L = 192 in L-band F-SAR full resolution data. For the C-band cells the standard deviation of ϕ_{ran} is 0.043 rad in case of $|\gamma|$ = 0.6 and 0.071 rad in case of $|\gamma|$ = 0.4.

During the F-SAR campaign the snowpack was dry with the exception of occasional transient melt-freeze events affecting the surface layer between some of the flights. This means that changes in CPD between flights may be attributed to the accumulation of fresh snow, to the formation of refrozen snow crusts or to other processes changing the snow microstructure. For dry snow CPD values are related to the depth-averaged structural anisotropy of the snowpack and are also affected by the polarization dependence of scattering on the underlying ground surface (Leinss et al., 2016; 2020). For the study period it can be assumed that the scattering properties at the ground surface did not change. In L-band the CPD values of the RoIs show little temporal variability, varying between -0.08 and -0.15 rad between individual flights. The analysis below refers to CPD of F-SAR C-band data.

https://doi.org/10.5194/egusphere-2026-2104
Preprint. Discussion started: 8 May 2026

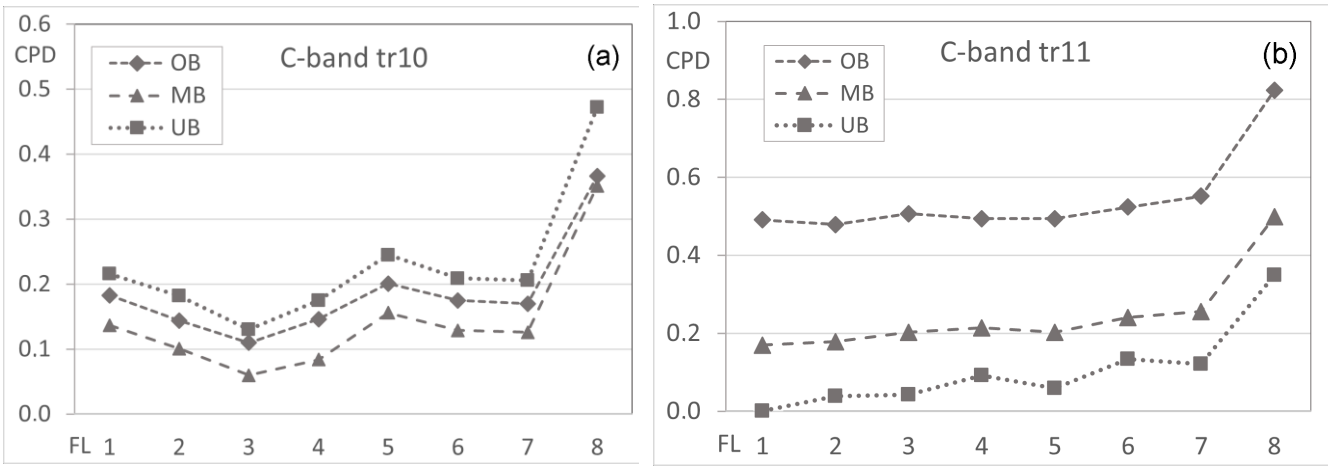

Figure 5: F-SAR C-band co-polarized phase difference (ϕ_{VV} - ϕ_{HH}) in radian, mean values of RoIs, flight 1 to flight 8. (a) track 10; (b) track 11. The CPD scales for (a) and (b) are different.

Figure 5 shows the temporal sequences of the C-band CPD for track 10 and track 11. The data points are average CPD values of the RoIs, based on cells of 25 x 25 pixels. Differences of the average CPD values between the RoIs and tracks can be primarily attributed to local phase differences of the signal reflected by the subnivean ground. The CPD differences between the two tracks can be explained by differences of the surface roughness on east- and west-facing slopes which are viewed under different local incidence angles depending on the track. CPD of rough soil increases with increasing incidence angle (Sarabandi, 1992; Oh et al., 2002). Such an effect is evident on OB where track 11 (θ_i = 37.4°) shows higher CPD than track 10 (θ_i = 28.3°). Between FL01 and FL07 the CPD values of track 10 and track 11 do not show major changes, but some variability. CPD of track 11 rises gradually from FL01 to FL07, overall by 0.09 rad, whereas track 10 shows some up and down. The variations of track 10 CPD between FL01 and FL07 may be the consequence of minor changes in the microstructure of the top snow layer due to wind effects and occasional solar illumination. After a drop of ΔCPD of 0.08 rad between FL01 to FL03 there is a rise of 0.10 rad between FL03 to FL05 and a drop of 0.03 rad between FL05 to FL07.

Whereas ΔCPD does not show a unique signal between FL04 and FL05, the timespan of SE1, there is a striking increase between FL07 (9 March) and FL08 (19 March) in track 10 (ΔCPD = 0.23) and in track 11 (ΔCPD = 0.25). The average depth of fresh snow (ΔSD) measured during this period along the snow transects amounted to 44 cm and the standard deviation of ΔSD at the measurement points was 5.7 cm. The ΔSD and ΔCPD samples of these points are uncorrelated (R^2 = 0.01). On the other hand, there is a distinct relationship between ΔCPD and the local incidence angle, with a coefficient of determination R^2 = 0.49 for linear regression (Fig.6). The slope of the regression line for the whole sample is 0.016 rad/degree. For the sub-sample with θ_i > 25° the slope is 0.030 rad/deg and the correlation increases to R^2 = 0.69.

https://doi.org/10.5194/egusphere-2026-2104
Preprint. Discussion started: 8 May 2026

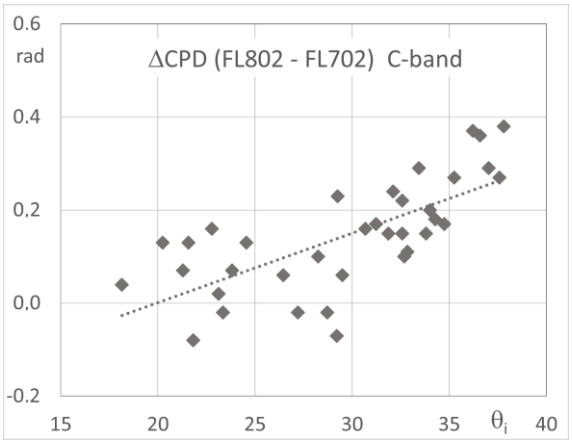

Figure 6: C-band co-polarized (VV-HH) phase difference (radian), F_SAR track 10, between FL07 and FL08 vs. radar incidence angle at in situ snow measurement points. The dashed line is the linear regression line.

On the days before FL08 the fresh snow layer had been subject to wind-induced fractionation and settling, processes inducing isotropic properties of snow structure. This explains the missing correlation between ΔSD and ΔCPD of FL07-FL08 and calls for another source than the fresh snow layer as driving factor for the increase of ΔCPD. The change of CPD and its increase with the incidence angle can be attributed to radar wave propagation through a frozen crust that developed on 11 March (two days after FL07) before the snowfall started, resulting in the formation of polycrystals with horizontal orientation (Kapil et al., 2010). Theory and experimental data show for horizontally aligned structures in snow positive values of the CPD, the magnitudes of which increase with the incidence angle (Leinss et al., 2016).

4. SWE retrieval by means of repeat-pass radar interferometry

The path delay of a radar signal propagating through a snow layer provides a basis for retrieving the depth and water equivalent of snow by means of differential radar interferometry (Guneriussen et al., 2001). In C-band and L-band impacts of absorption and scattering losses in dry seasonal snow can be neglected for DInSAR based SWE retrievals. Critical issues are the 2π phase ambiguity and the temporal decorrelation of the interferometric phase for which snowfall intensity and melting are decisive factors. We studied different options for coping with these issues, put forward in this section.

The change in snow depth (Δd_s) due to accumulation of snow on a ground surface or on top of a seasonal snowpack can be derived from measurements of the interferometric phase before and after the snowfall. The interferometric phase difference due to snow accumulation can be described by (Guneriussen et al., 2001):

$$\Delta\phi_s = -2k\Delta d_s\left(\cos\theta_i - \sqrt{\varepsilon_s - \sin^2\theta_i}\right) \quad (5)$$

where ε_s is the dielectric permittivity of the snowpack, θ_i is the local incidence angle and k is the wavenumber in free space. An estimate for the density, ρ, of the accumulated snow is needed for computing ε_s and for deriving ΔSWE from snow depth:

https://doi.org/10.5194/egusphere-2026-2104
Preprint. Discussion started: 8 May 2026

$$\Delta SWE = \Delta d_s\, \rho = -\Delta\phi_s\ \rho\ \frac{\lambda}{4\pi}\left[1\Big/(\cos\theta_i - \sqrt{\varepsilon_s - \sin\theta_i^2})\right] \quad (6)$$

For dry snow the imaginary part of the microwave permittivity can be neglected. The real part can be estimated as a function of the snow density (Wiesmann and Mätzler, 1999):

$$\varepsilon_s' = 1 + 1.60\,\rho + 1.86\,\rho^3, \qquad \rho \le 0.40 \text{ g cm}^{-3} \quad (7)$$

For dry seasonal snow at incidence angles ≤ 40° the snow density has only a small impact on the sensitivity of the interferometric phase delay in respect to SWE. Under these constraints a linear approximation can be applied for deriving ΔSWE from $\Delta\phi_s$ that does not account for different snow densities:

$$\Delta SWE = \Delta d_s\, \rho \approx \frac{\lambda}{2\pi} f_s\, \Delta\phi_s \cos\theta_i\ \ [mm] \quad (8)$$

We use this relation for computing the error estimates for ΔSWE. For snow density ρ ≤ 0.4 g cm^{-3} and $\theta_i \le 40°$ the scaling factor f_S is 0.654. λ is the radar wavelength in mm. ΔSWE values computed by Eq. 8 differ by no more than ± 3% from the ΔSWE values computed by Eq. 6.

In situ snow depth and SWE measurements refer to the vertical direction also on slopes (Fierz et al., 2009). For deriving Δd_s and ΔSWE from the observed phase on sloping terrain, the slope angle, α, needs to be taken into account:

$$\Delta SWE = -\Delta\phi_s\ \rho\ \frac{\lambda}{4\pi}\ \frac{1}{\cos\alpha}\ \frac{1}{\cos\theta_i - \sqrt{\varepsilon_s - \sin\theta_i^2}} \quad (9)$$

In order to derive the change in phase attributed to changes in snow mass, $\Delta\phi_s$, from the total phase difference, $\Delta\phi_t$, in repeat pass interferograms, it is necessary to eliminate phase terms that are induced by other processes. A convenient option is the use of a reference phase at sites without change in snow mass or with in situ measurements of ΔSD or ΔSWE if available within the scene:

$$\Delta\phi_s = \Delta\phi_t - \Delta\phi_{ref} \quad (10)$$

Error estimates for retrieved snow depth and SWE need to account for the random phase error of the snow pixel ($\Delta\phi_{s.ran}$) and of the reference target ($\Delta\phi_{ref}$), combined in quadrature:

$$\sigma_{\phi S}(x,y) = \sqrt{\sigma^2_{\phi s,ran}(x,y) + \sigma^2_{\phi,ref}(x,y)} \quad (11)$$

The random phase error can be computed in dependence of coherence and number of samples according to Eq.4. In case of Eq. 8 the resulting error for ΔSWE can be computed by:

$$\sigma(\Delta SWE) = \frac{\lambda}{2\pi} f_S \cos\theta \sqrt{\sigma^2_{\phi s,ran}(x,y) + \sigma^2_{\phi,ref}(x,y)} \quad (12)$$

https://doi.org/10.5194/egusphere-2026-2104
Preprint. Discussion started: 8 May 2026

For the Wörgetal ΔSD and ΔSWE retrievals we use the phase of the corner reflectors cleaned of snow (ΔSWE = 0) as reference. The $\Delta\phi$ values of individual corner reflectors along a given flight track show some differences, possibly caused by imperfect squint corrections due to variable wind conditions along the track. Sidelobes from terrain surrounding the corner reflector may also play a role, in particular in L-band. The corner reflector phase is derived from single full resolution pixels so that the maximum likelihood estimator for computing the random phase error cannot be applied. As estimate for the uncertainty of the corner reflector phase, we use the maximum absolute deviation of the phase of a single reflector, $\delta_{\Phi,CR}$, within a scene from the mean ϕ value of the reflectors.

In addition to the errors specified in Equ. 12, systematic errors from other sources may play a role. The magnitude of the random error can be reduced by increasing the estimation cell size, whereas systematic errors cause phase offsets affecting sections of a scene or the whole scene. A possible source are residual baseline errors, impacts of which depend on the steepness of the terrain. The Wörgetal RP-InSAR data show reduced coherence and increased phase uncertainties on steep slopes that may be attributed to imperfect corrections of the topographic phase resulting from smoothing effects and errors in the DEM or from disturbances caused by varying wind conditions.

4.1 SWE retrievals based on full resolution F-SAR data

Coherence estimates and ΔSWE retrievals with the full resolution F-SAR data are based on cells of 25 x 25 pixels. The coherence is a critical parameter for estimating the phase uncertainty and SWE retrieval errors. Table 5 shows the average C-band and L-band coherence values of the RoIs for RP-InSAR scenes spanning the two snowfall events. The minimum time span of F-SAR flights covering SE1 (FL04-FL05) is two days (4 to 6 March) and for SE2 (FL07-FL08) 10 days (9 to 19 March). In both cases the snowpack of the RoIs was dry during the radar data acquisition. Figure 7 shows C-band and L-band coherence images of periods spanning the two snowfall events. In the Supplement (Fig. S7) we show coherence images for a time span without snowfall (FL03-FL04) for both frequencies.

The coherence images show low coherence on steep slopes also for time spans without snowfall (Fig. S7). This is probably caused by uncertainties in the topographic phase. Snowfall events cause major decrease of coherence in C-band. For dry snow the main reason for decorrelation due to the accumulation of dry snow is the differential change of the path of the radar signal propagating through a snow layer above a rough ground surface (Rott et al., 2004, Lei et al., 2016)). Due to the reduced sensitivity to changes in snow depth, L-band is less affected by temporal decorrelation than C-band. For the interferograms spanning SE1 the C-band the drop in coherence of the RoIs is not large, declining on average from $|\gamma| = 0.940$ for a period without snowfall (FL02 to FL03) to $|\gamma| = 0.788$ for FL04 to FL05. The SE2 coherence of C-band is low, the average $|\gamma|$ value is 0.376. The L-band coherence values are much higher: $|\gamma| = 0.942$ for SE1 and $|\gamma| = 0.764$ for SE2. VV-polarization shows in both radar frequencies slightly higher coherence than HH-polarization. UB has lower coherence than OB and MB in both frequencies, with the lowest value in C-band SE2.

https://doi.org/10.5194/egusphere-2026-2104
Preprint. Discussion started: 8 May 2026

Table 5. Coherence magnitude of the RoIs derived from C-band and L-band full resolution F-SAR data spanning the snowfall events SE1 (FL04-FL05) and SE2 (FL07-FL08). Mean values of track 10 and track 11.

	SE1				SE2			
Site	C-HH	C-VV	L-HH	L-VV	C-HH	C-VV	L-HH	L-VV
OB	0.829	0.852	0.943	0.944	0.462	0.484	0.840	0.854
MB	0.790	0.822	0.942	0.953	0.435	0.464	0.813	0.838
UB	0.701	0.738	0.932	0.942	0.198	0.217	0.608	0.634
Mean	0.773	0.804	0.939	0.946	0.365	0.388	0.754	0.775

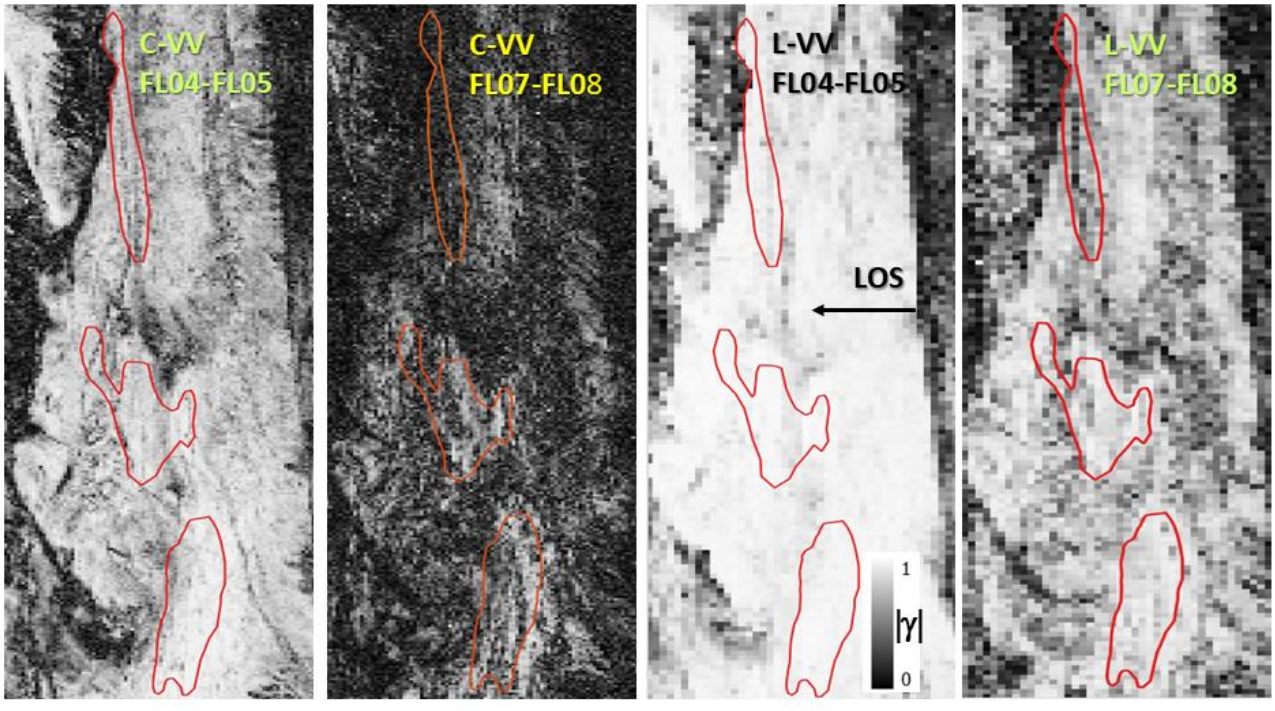

Figure 7: F-SAR repeat-pass interferometric coherence magnitude |γ|, images in radar geometry. C-band VV and L-band VV, track 10, image pairs FL04-FL05 (SE1), and FL07-FL08 (SE2). LOS radar line-of-sight.

Table 6 provides error estimates for ΔSWE according to Equ. 12 for an incidence angle of 30°, accounting for the random error of the interferometric phase of snow and for the error estimate of corner reflectors. Mean coherence values of the three RoIs at HH and VV polarisation are used for computing the random phase errors of the snow pixels. $\delta_{\phi,CR}$ is the maximum absolute deviation of the corner reflector phase of the InSAR scenes that are used for computing ΔSWE.

https://doi.org/10.5194/egusphere-2026-2104
Preprint. Discussion started: 8 May 2026

Table 6. Error estimates for the interferometric phase of snow ($\sigma_{\phi,ran}$, cell size 25 x 25 pixels), phase error for the corner reflectors ($\delta_{\Phi,CR}$), and resulting error estimate for ΔSWE, at θ_i =30°. $|\gamma|$ is the average coherence magnitude of HH and VV polarized F-SAR data of the three RoIs.

Event	Frequency	$\|\gamma\|$	$\sigma_{\phi,ran}$ rad	$\delta_{\Phi,CR}$ rad	σ(ΔSWE) mm
SE1	C-band	0.788	0.045	0.308	1.57
SE1	L-band	0.942	0.018	0.119	2.43
SE2	L-band	0.764	0.044	0.329	6.71

Due to the large number of looks the random phase error of the snow pixels is low and the ΔSWE uncertainty is dominated by the error of the reference phase. C-band has higher sensitivity of the RP-InSAR phase in respect to SWE and is therefore less affected by uncertainties of the corner reflector phase. On the other hand, C-band suffers from 2π phase ambiguity in case of high snow accumulation (Figure S8) and the coherence is low in case of intense snowfall. At 50° incidence angle the phase sensitivity in respect to ΔSWE for fresh snow (ρ_s = 0.1 g cm^{-3}) is in C-band 0.255 rad/mm and in L-band 0.0637 rad/mm, yielding 2π phase ambiguities for ΔSWE of 26.6 mm in C-band and 98.6 mm in L-band. The snowfall amount of SE2 exceeds the C-band 2π phase ambiguity up to three-fold. Therefore, we use C-band data only for ΔSWE retrievals of snowfall SE1.

In case of SE1 there are several options for combining flights spanning the event, whereas for SE2 two combinations are available, FL06-FL08 and FL07-FL08. As evident from the error estimates for ΔSWE retrievals (Table 6), the main source of uncertainty is the CR phase. We checked the phase of the CRs for the available RP-InSAR pairs spanning the two snowfall events and selected the RP-InSAR pairs with minimum phase error. Based on these checks, the following RP-InSAR pairs were used for ΔSWE retrievals: for SE1 track 10 FL03-FL06, for SE1 track 11: FL01-FL05; for SE2 track 10 and track 11: FL07-FL08.

Figure 8 shows wrapped phase images of interferograms used for ΔSWE retrievals. The phase values $\Delta\phi_s$ are directly related to ΔSWE as they represent the difference in respect to the corner reflector phase. The colour scale for C-band SE1 and L-Band SE2 covers one full phase cycle. The colour scale for L-band SE1 covers one quarter of a phase cycle, reflecting the different phase sensitivity of the two wavelengths. The central section of Wörgetal is not subject to 2π phase ambiguities in both C- and L-band in case of SE1 and in L-band also in case of SE2. On steep fore-slopes, and on backslopes with incidence angles larger than about 60° the phase is noisy.

ΔSWE is derived from $\Delta\phi_s$ by means of Eq. 9. For computing the permittivity and converting the computed Δd_s into ΔSWE snow density ρ = 0.1 g cm^{-3} is used for SE1 and ρ = 0.145 g cm^{-3} for SE2. The difference in computed ΔSWE amounts only to 0.9% using either of the two densities. The impact of the slope correction term (1/cos α in Eq. 9) within the RoIs is also small. On the average over the RoIs the slope correction term results in an increase of ΔSWE by 1.0 %.

https://doi.org/10.5194/egusphere-2026-2104
Preprint. Discussion started: 8 May 2026

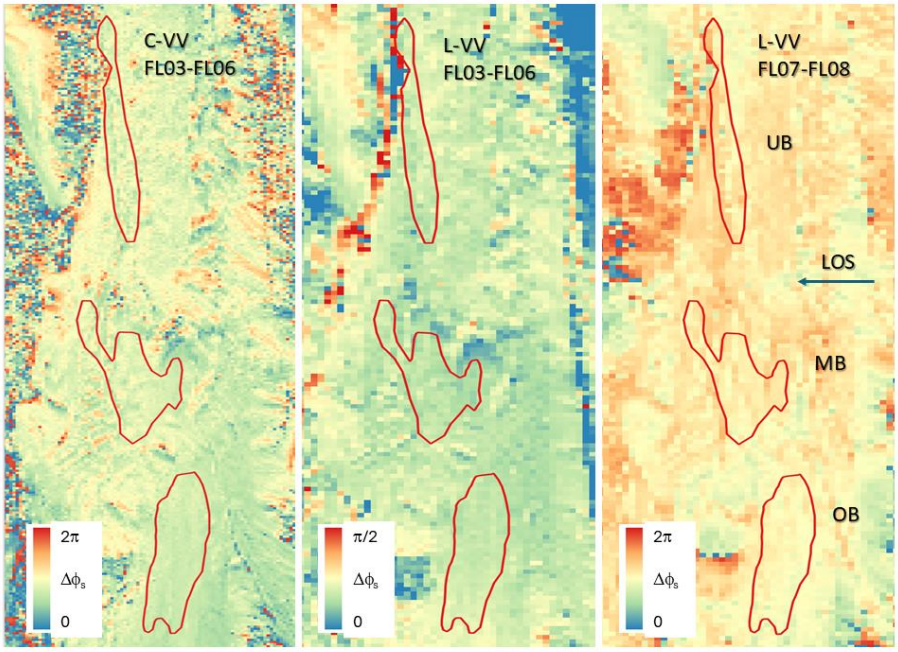

Figure 8: F-SAR track 10 wrapped phase images ($\Delta\phi_s$) of RP InSAR scenes spanning SE1 (C_{VV} and L_{VV}) and SE2 (L_{VV}), in radar imaging geometry. $\Delta\phi_s$ is the phase difference due to fresh snow. LOS: radar line-of-sight. Different range of the colour scale for SE1 (FL03-FL06) in C-band and L-band.

The ΔSWE images (Fig. 9) show a smooth pattern in the level sections of Wörgetal and get noisy with increasing steepness of slopes. The steep lateral slopes of the valley that are facing the radar are largely shorted and cannot be used for SWE retrievals. This is evident by comparing the ΔSWE image in radar geometry with a ΔSWE image in map projection (Fig S9) in which zones with of layover and incidence angles < 15° are uncovered. Steep backslopes with incidence angles > 70° are also outlined but these affect a smaller part of the radar image than the steep foreslopes.

Figure 10 shows a scatterplot of the computed ΔSWE values of RoIs versus in situ measurements. The in situ numbers for the RoIs are based on point measurements along transects, whereas F-SAR ΔSWE is derived from phase data providing full spatial coverage. Consequently, part of the differences between the two samples can be attributed to different spatial coverage. Numerical values of the computed ΔSWE values of the RoIs, derived from VV- and HH-polarized data, are specified in the Supplement (Table S1). The average differences in ΔSWE derived from HH and VV polarized data of SE1 are small, amounting in C-band to 0.1 mm and in L-band to 0.2 mm. For SE2 (L-band) the average difference in ΔSWE from HH and VV data is 1.9 mm, corresponding to 3% of the ΔSWE value.

https://doi.org/10.5194/egusphere-2026-2104
Preprint. Discussion started: 8 May 2026

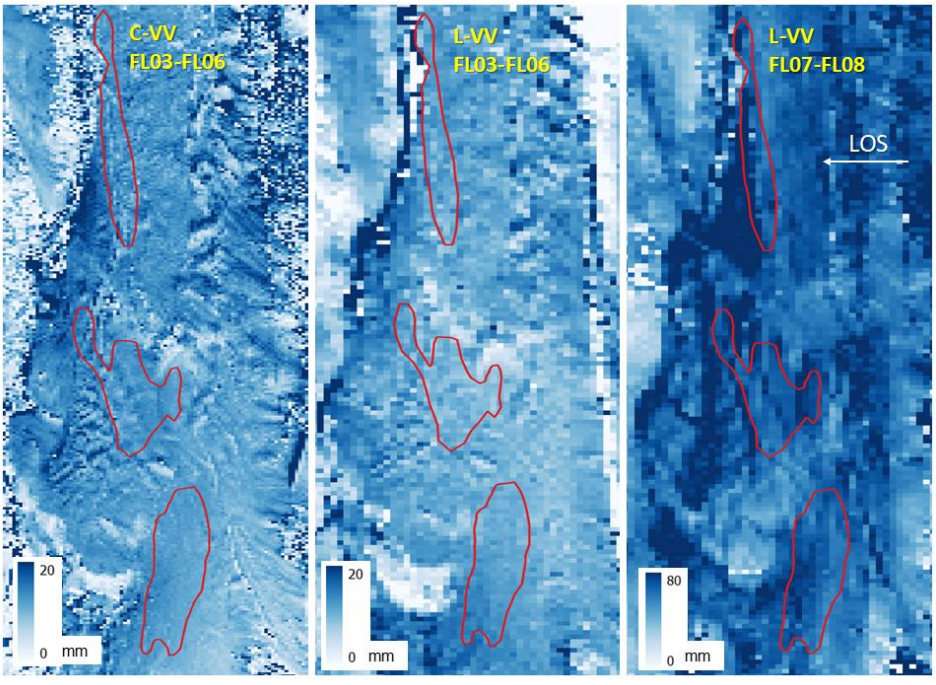

425 **Figure 9: ΔSWE of snowfall events, derived from InSAR data of track 10, for SE1 from FL03-FL06 C_{VV} and L_{VV}, for SE2 from FL07-FL08 L_{VV}. Colour scale for ΔSWE: 0 mm to 20 mm for SE1, 0 mm to 80 mm for SE2.**

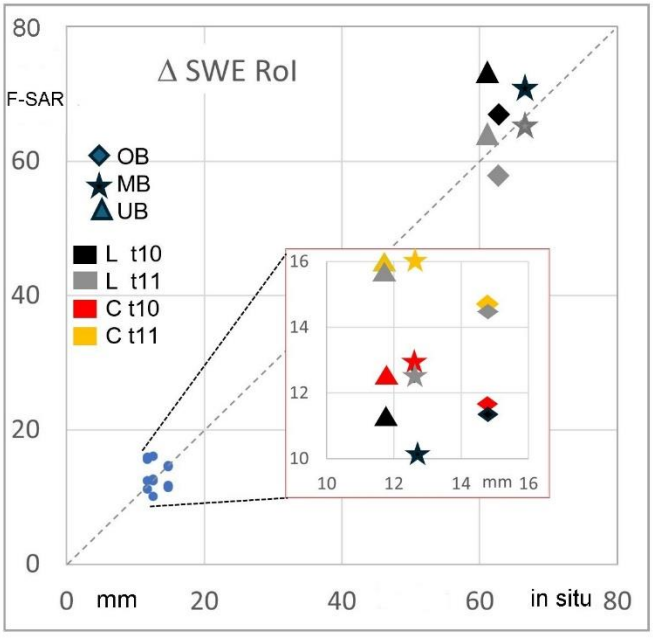

Figure 10: Scatterplot of ΔSWE values of the RoIs derived from F-SAR L-band VV and C-band VV InSAR data, track 10 and track 11, versus in situ measurements.

https://doi.org/10.5194/egusphere-2026-2104
Preprint. Discussion started: 8 May 2026

For SE1 the C-band and L-band ΔSWE retrievals show similar performance. The average ΔSWE value of the three RoIs, derived from C-band data, amounts to 14.3 mm, the mean root mean square difference (RMSD) of the 12 cases (2 polarizations, 2 tracks, 3 RoIs) is 2.7 mm. The mean ΔSWE value from L-band data is 12.6 mm, the RMSD 2.5 mm. The in situ ΔSWE value is 13 mm. On the other hand, the differences between the individual tracks are larger. SE1 ΔSWE of C-band track 11 exceeds that of track 10 by 3.2 mm, and SE1 ΔSWE of L-band track 11 exceeds that of track 10 by 3.4 mm. The difference between the two tracks can be attributed to biases of the corner reflector phase. During the flights the prevailing wind direction was from west to east, resulting in opposite signs of the squint angle for the two tracks. The mean in situ ΔSWE value of the RoIs for SE2 amounts to 63.4 mm, the corresponding value of L-band based ΔSWE from both polarizations amounts to 65.0 mm, the RMSD of the 12 cases is 4.9 mm. The difference between mean ΔSWE of the two tracks is 7.6 mm. Also, in this case the squint angles of the two tracks had opposite signs because of crosswind.

For SE1 the spatial variability of the ΔSD point sample is small: the mean ΔSD of in situ transects is 14.1 cm, the standard deviation of ΔSD at the points is 2.4 cm. For SE2 the ΔSD magnitude and variance of SE2 are higher. The mean in situ ΔSD amounts to 44.6 cm, the standard deviation of the point sample is 5.6 cm. Figure S10 shows a scatterplot of ΔSD in situ point measurements versus co-located ΔSD retrievals for SE2, derived from L-band VV data of track 10 FL07-FL08. In order to minimize impacts of uncertainties related to the topographic phase, the ΔSD sample in Fig. S10 is confined to incidence angles between 15 and 40 degrees. The mean computed ΔSD is overestimated by 1.7 cm, the RMSD of the point sample is 5.0 cm. Differences can partly be attributed to the size of the ΔSD cells: in situ 3 m x 3 m, F-SAR L-band 10 m x 30 m (azimuth x ground range) at $\theta_i = 30°$.

4.2 SWE retrieval by means of split-bandwidth radar interferometry

In order to minimize errors and constraints arising from 2π phase ambiguities Engen et al. (2004) proposed the use of the Delta-k interferometric method for deriving SWE from repeat-pass InSAR data. SWE retrievals by means of Delta-k apply the same concept as the conventional repeat-pass InSAR approach based on differential phase delay estimation, replacing the wavenumber in Eqs. 5 to 9 by Delta-k, the differential wavenumber of a radar system with dual frequencies. In case of split-bandwidth interferometry each of the two complex SAR images, s_1 and s_2, used for generating the interferogram, is split into a lower and an upper range band-pass filtered version: $s_{1,l}$, $s_{1,u}$ and $s_{2,l}$, s_{2u} (Bamler and Eineder, 2004; 2005). Interferograms are generated for the lower and upper sub-band images:

$$\phi_l = \angle\,(s_{1,l} \cdot s_{2,l}^*) \quad ; \quad \phi_u = \angle\,(s_{1,u} \cdot s_{2,u}^*) \tag{13}$$

A differential interferogram is formed, representing the pixel-wise phase difference of the two interferograms:

$$\Delta\phi(\Delta k) = \phi_l - \phi_u = \angle\left[\left(s_{1,l} \cdot s_{2,l}^*\right) \cdot \left(s_{1,u} \cdot s_{2,u}^*\right)^*\right] \tag{14}$$

https://doi.org/10.5194/egusphere-2026-2104
Preprint. Discussion started: 8 May 2026

The frequency separation of a split-bandwidth system determines the sensitivity in respect to measurements of phase differences. For the Delta-k SWE retrieval by means of the F-SAR data we split the total range bandwidth in C-band (B = 384 MHz) into lower and upper sub-bands of b = 100 MHz bandwidth. In L-band the total bandwidth (B = 150 MHz) is split into lower and upper sub-bands of b = 50 MHz bandwidth (Table 7). The number of sub-band resolution elements is given by: $N_b = N_L \cdot (b/B)$. For the selected split-bandwidth ratio the range resolution is reduced by a factor of 3.84 in C-band and a factor of 3.0 in L-band compared to the full resolution data.

Table 7. Bandwidth and Δk wavenumber for F-SAR split-bandwidth InSAR retrievals of Wörgetal. B – F-SAR total range bandwidth, b -bandwidth of the lower and upper sub-band. The sensitivity ΔSWE/Δk refers to snow with density ρ= 0.3 g cm^{-3} at a radar incidence angle θ_i = 30°.

Channel	B	b	Δk	ΔSWE/Δk
	MHz	MHz	m^{-1}	mm/rad
C-band	384	100	5.95	95.0
L-band	150	50	2.10	269.6

Placing the sub-bands in the upper and lower bounds of the full system bandwidth and assuming that the central frequency of the sub-band is its carrier frequency, the split-bandwidth frequency separation is 284 MHz in C-band and 100 MHz in L-band. The sensitivity of the Δk interferometric phase in respect to ΔSWE is largely reduced compared to interferograms that are using the wavenumber of full bandwidth data. The differences in sensitivity of the phase in respect to ΔSWE between the full bandwidth and the Delta-k approach depend on the ratio of the wavenumbers (k/Δk), amounting to 18.70 in C-band and 13.25 in L-band. For the full resolution F-SAR data the sensitivity of the phase in respect to SWE of C-band exceeds 4.0 times that of L-band, in accordance with the inverse wavelength ratio. For Delta-k the ratio of the C-band to L-band sensitivity is 2.84, according to the ratio of the split-bandwidth separations. An example for the Δk sensitivity in respect to ΔSWE is specified in Table 7.

Figure 11 shows the relation between the Δk phase and ΔSWE in dependence of the incidence angle for the F-SAR case with snow densities ρ = 0.15 g cm^{-3} and ρ = 0.30 g cm^{-3}. For incidence angles between 20° and 45° the differences between the two snow densities are small. A 2π phase shift (for snow with ρ = 0.30 g cm^{-3}) corresponds in C-band at θ_i = 20° to ΔSWE = 637 mm and at θ_i = 70° to ΔSWE = 343 mm. The corresponding numbers in L-band are 1810 mm and 975 mm. In order to achieve suitable performance of computed ΔSWE high accuracy of the Δk phase is needed. This implies retrieval cell sizes comprising a large number of independent samples. The split-bandwidth interferometric phase error can be estimated according to the formulation of Bamler and Eineder (2005):

$$\sigma_{split} = \frac{1}{2\pi}\frac{B}{B-b}\sqrt{\frac{B}{b}}\frac{1}{\sqrt{N}}\frac{\sqrt{1-\gamma^2}}{\gamma} \quad (15)$$

https://doi.org/10.5194/egusphere-2026-2104
Preprint. Discussion started: 8 May 2026

The performance estimation according to this equation is close to the accuracy estimate using the Cramér–Rao bound (Bamler and Eineder, 2004; 2005). Figure 12 shows estimates for the ΔSWE retrieval error due to random phase noise in dependence of the number of independent samples. The reduced performance of L-band compared to C-band for a given coherence value results from the lower Δk number. On the other hand, the coherence in L-band is less affected by decorrelation in case of snowfall than in C-band. For example, the error estimates for C-band $|\gamma| = 0.30$ show the same phase-related uncertainty as for L-band $|\gamma| = 0.66$. The larger susceptibility to temporal decorrelation of C-band limits the potential gain by the higher phase-sensitivity in respect to SWE.

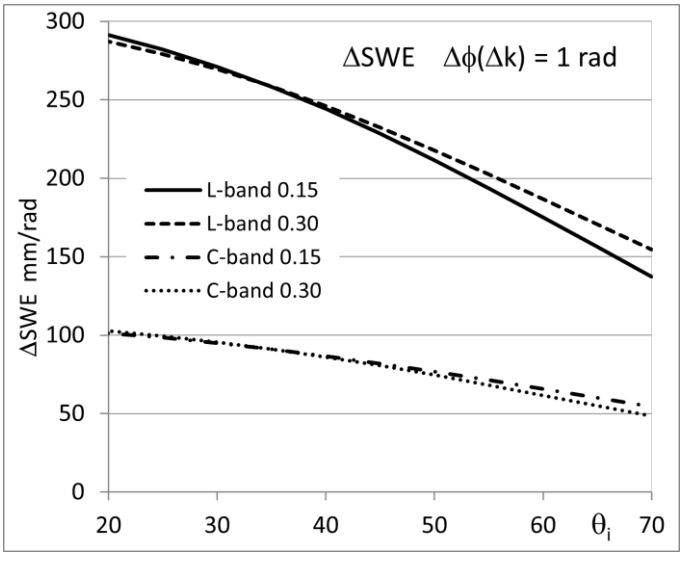

Figure 11: ΔSWE values corresponding to a Δk phase difference of one radian in dependence of the radar incidence angle, for Δk C-band and L-band properties specified in Table 7, assuming snow densities ρ of 0.15 g cm^{-3} and 0.30 g cm^{-3}.

For the performance analysis of F-SAR Δk SWE retrievals we use cells of 51 x 51 pixels in C-band and 25 x 25 pixels in L-band. These cells are of similar extent in azimuth x range: 10.2 m x 15.3 m in C-band and 10 m x 15 m in L-band. The resulting number of resolution elements for the selected F-SAR split-bandwidth windows of this size is: $N_b = 163$ in C-band, $N_b = 64$ in L-band. For the Δk SWE retrievals of SE1 we use only C-band data because the sensitivity of L-band Δk is not suitable for sensing low snow amounts. For SE2 we performed ΔSWE retrievals for both frequencies. For computing the Δk phase difference images spanning the snowfall events we used InSAR pairs for which the differences in Δk phase between individual reflectors are minimum, for SE1 C-band track 10 FL03 – FL06 and track 11 FL01- FL05; for SE2 C-band and L-band: track 10 FL06 – FL08, track 11 FL07- FL08.

https://doi.org/10.5194/egusphere-2026-2104
Preprint. Discussion started: 8 May 2026

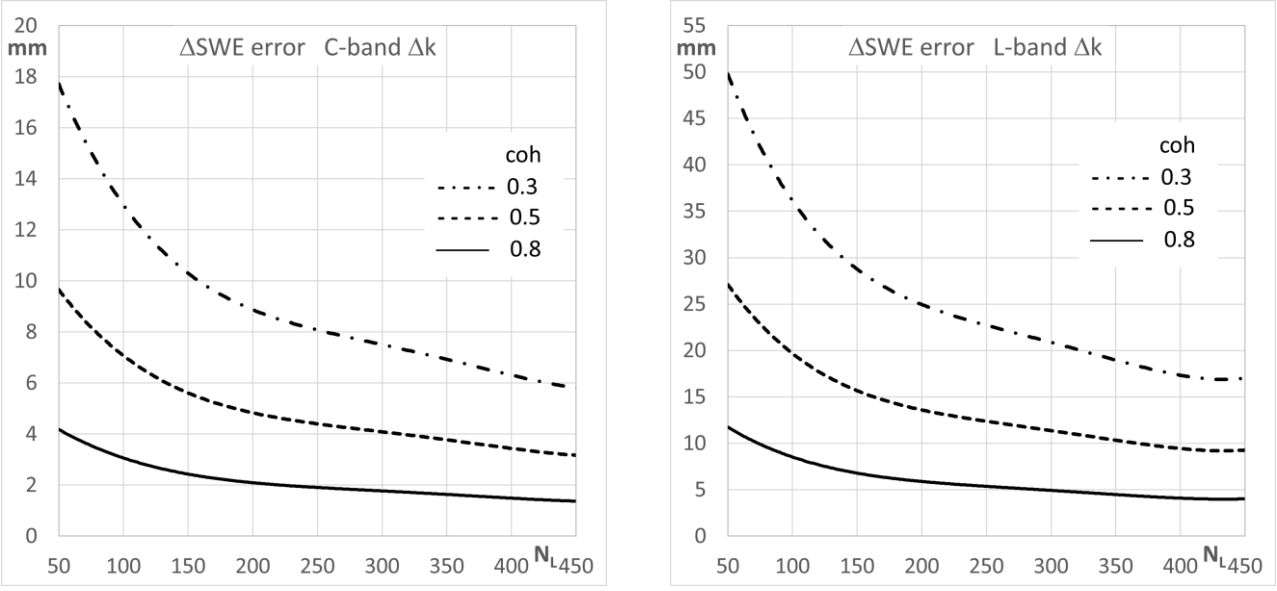

505 **Figure 12: ΔSWE error (standard deviation) in mm water equivalent due to random phase noise in dependence of the number of independent samples (N_L) for Δk InSAR retrievals using C-band and L-band specifications in Table 7, for different values of the coherence magnitude. Incidence angle θ_i = 30°, snow density ρ = 0.3 g cm^{-3}.**

Table 8 shows the sub-band coherence magnitudes of the RoIs for the snowfall events SE1 and SE2, based on the scenes specified above. The comparison with the full bandwidth RP-InSAR coherence values (Table 5) is in high agreement for L-
510 band SE2, pointing out that in this case the reduced bandwidth does not have an impact. The C-band Δk coherence of SE1 is on average 10% lower than the full bandwidth coherence. The differences are largest in UB which shows in general lower coherence than the two other sites. A similar trend is evident for the C-band data of SE2, the average Δk coherence of which is on average 20% lower than the full bandwidth coherence. The spatial pattern of Δk coherence (Fig. S11) resembles that of the full bandwidth coherence (Fig. 7).

515 **Table 8. RoI coherence magnitude of split-bandwidth sub-bands spanning the snowfall events SE1 and SE2. Mean values of track 10 and track 11.**

	SE 1		SE 2			
Site	C-HH	C-VV	C-HH	C-VV	L-HH	L-VV
OB	0.792	0.812	0.378	0.397	0.831	0.854
MB	0.721	0.749	0.347	0.372	0.810	0.833
UB	0.596	0.614	0.146	0.159	0.613	0.631
Mean	0.703	0.725	0.290	0.309	0.751	0.773

For retrieving ΔSWE from the Δk phase differences we apply the same procedures as for the conventional DInSAR approach. Error estimates for the Δk SWE retrievals are shown in Table 9, based on average phase errors for the RoIs and reflectors. As

https://doi.org/10.5194/egusphere-2026-2104
Preprint. Discussion started: 8 May 2026

for the conventional RP-InAR case (Table 6) the error of the reflector phase, used as reference for zero ΔSWE, has a larger share in the total uncertainty than the random phase error. The lower number of looks for the L-band Δk cells compared to C-band is also of relevance, but for the random phase error this is partly compensated by the higher L-band coherence. The ΔSWE error estimates for Δk are about four times higher than corresponding estimates for the full resolution data. This can mainly be attributed to the lower sensitivity of the Δk phase in respect to SWE.

Table 9. Error estimates for the F-SAR based Δk interferometric phase, cell size in C-band 51 x 51 pixels, in L-band 25 x 25 pixels, incidence angle 30°. $|\gamma|$ is the average coherence magnitude of HH and VV polarized Δk InSAR data of the RoIs. $\delta_{\Phi,CR}$ is the error of the reflector phase.

Event	Frequency	$\|\gamma\|$	$\sigma_{\Phi,ran}$ rad	$\delta_{\Phi,CR}$	σ(ΔSWE) mm
SE1	C-band	0.714	0.024	0.051	5.38
SE2	C-band	0.300	0.105	0.112	14.61
SE2	L-band	0.762	0.044	0.098	28.98

ΔSWE images are shown in Fig. 13 and ΔSWE values of the RoIs are listed in in Table S2. A coherence threshold was applied for the Δk SWE retrievals, excluding cells with $|\gamma| < 0.3$. Due to the low coherence and the constraint, the number of valid C-band ΔSWE cells for SE2 in UB is less than 5% of the total number, an insufficient sample for reliable ΔSWE estimates. Therefore, we do not provide C-band ΔSWE numbers on UB for SE2. For C-band SE1 the percentage of valid pixels ($|\gamma| \geq 0.3$) is at least 98 % and for C-band SE2 the numbers for OB and MB range from 50 % to 67 %, depending on the RoI, track and polarization. For L-band SE2 the percentages of valid pixels in individual RoIs range from 91% to 99 %.

The average differences of computed ΔSWE between HH and VV polarization are small, 0.8 mm in C-band SE1, 0.4 mm in C-band SE-2 and 2.4 mm in L-band SE2 (Table S2). The overall mean ΔSWE of SE1, based on C-band data of both tracks, exceeds the in situ values by 2.0 mm. The C-band retrievals for SE2 underestimate the mean ΔSWE of OB and MB by 12.6 mm, the L-band retrievals show an overestimation by 5.0 mm for the three RoIs. The C-band ΔSWE data of SE2 suffer from the limited number of valid pixels due to low coherence. For individual sites and tracks the deviations of ΔSWE from in situ observations are larger. Biases in the reference phase are a main reason for the differences in computed ΔSWE between the two tracks, as it is the case for the full resolution F-SAR data.

https://doi.org/10.5194/egusphere-2026-2104
Preprint. Discussion started: 8 May 2026

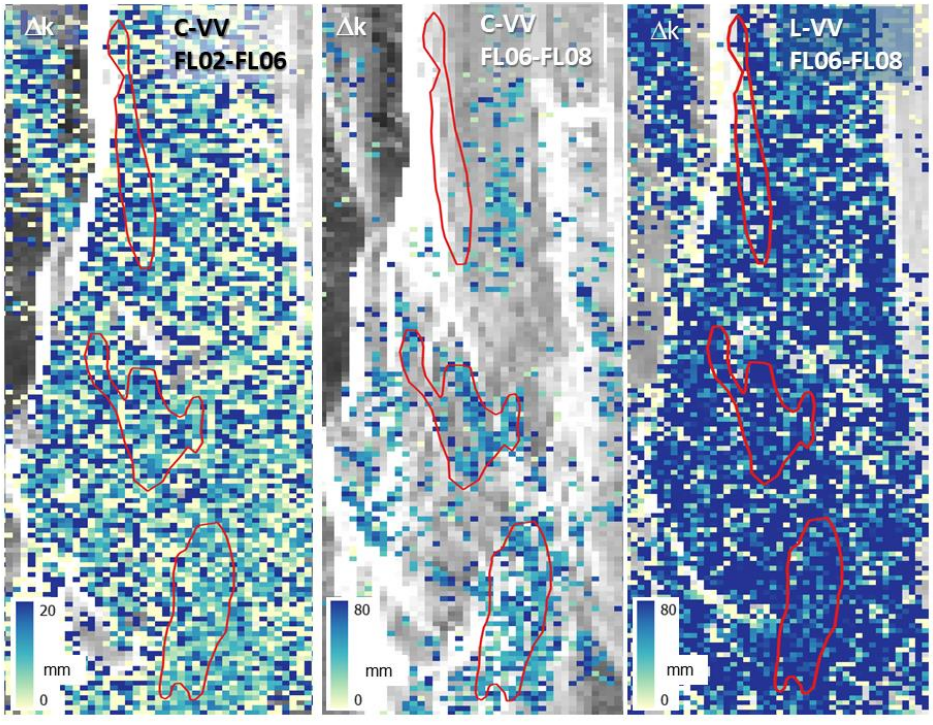

Figure 13: ΔSWE images of snowfall events SE1 (C_{VV}) and SE2 (C_{VV} and L_{VV}) track 10, in radar imaging geometry, derived from F-SAR Δk data. The ΔSWE colour scale for SE1 ranges from 0 mm to 20 mm and for SE2 from 0 mm to 80 mm. Background: SAR amplitude images.

4.3 SWE retrievals using simulated geosynchronous SAR data

The feasibility study on the use of geosynchronous SAR for SWE monitoring is based on simulated geosynchronous SAR data that reflect the properties of the proposed Earth Explorer 10 mission candidate Hydroterra (ESA, 2020; Hydroterra Mission Team, 2020). The simulated geosynchronous SAR products are in the following labelled Hydroterra (HT) products. For Hydroterra a C-band SAR in single polarization mode (HH) has been proposed. In the study simulated products were also generated for VV polarization. Differences between the simulated HT SAR products and those of full resolution and Delta-k data are the lower range and azimuth resolutions (Table 10), the lower NESZ, and the use of longer integration time for generating SAR images. Simulated HT interferometric products were derived from data of the following F-SAR flights that are spanning snowfall events: FL01 - FL05 (SE1) and FL02 – FL08 (SE1 and SE2). The interferometric signals between FL02 and FL08 exceed the 2 π phase ambiguity up to 3-fold and have low coherence. Therefore, the analysis in this section deals with the simulated data for SE1.

Long integration time for SAR image focusing is applied in order to simulate the slow velocity of a satellite in geosynchronous orbit in respect to the observed section of the Earth surface (Gracheva et al., 2021). The integration time for the simulated

https://doi.org/10.5194/egusphere-2026-2104
Preprint. Discussion started: 8 May 2026

FL01 HT SAR scene is 106 minutes and for the FL05 scene 110 minutes. The long integration times could be achieved because each of the F-SAR flight sorties FL01 and FL05 included 11 repeat passes.

Table 10. Specifications of parameters of the simulated Hydroterra products.

Centre frequency	5300 MHz
Range bandwidth	6 MHz
Noise equivalent sigma zero	-21.2 dB
Azimuth resolution (single look)	5 m
Slant range resolution (single look)	22.2 m
Pixel size (azimuth x range)	2.93 m x 19.18 m

In order to obtain ΔSWE maps with a spatial resolution that provides an adequate number of cells for each RoI we used a cell size of 10 x 1 pixels (azimuth x range). This cell size corresponds to a surface area of 29.3 m x 38.4 m at $\theta_i = 30°$. The number of independent samples (N_L) is 5.1. Figure 14 shows simulated HT images of the coherence magnitude and ΔSWE derived from the FL01 - FL05 images. The numbers for coherence and computed ΔSWE of the RoIs are listed in Table 11.

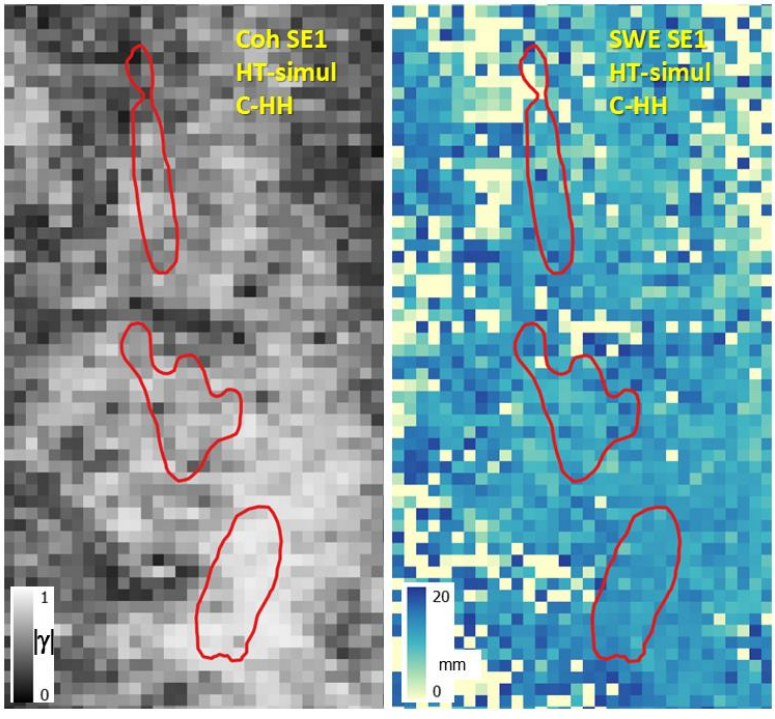

Figure 14: Simulated Hydroterra SAR images of coherence magnitude and ΔSWE for snowfall event SE1, derived from F-SAR data of track 10.

https://doi.org/10.5194/egusphere-2026-2104
Preprint. Discussion started: 8 May 2026

The comparison of coherence images of SE1 shows for the simulated HT image a similar pattern as for the full resolution RP-InSAR coherence (Fig. 8), with low coherence on steep slopes. In OB the coherence is rather high in both cases: 0.834 for HT and 0.840 for full resolution InSAR. UB shows the largest drop, with average $|\gamma| = 0.540$ for HT vs. $|\gamma| = 0.719$ for full resolution InSAR. A reason for the reduced coherence of the HT products is the lower spatial resolution which affects the co-registration of the repeat-pass pairs, in particular on rugged terrain and on steep slopes. The VV coherence exceeds the HH coherence on average by 3%, a similar number as for the coherence of the full resolution data.

Table 11. RoI coherence magnitude and ΔSWE (in mm) of snowfall event SE1 in simulated Hydroterra SAR images derived from F-SAR data of track 10 and track 11, HH and VV polarizations.

	COH t10		COH t11		ΔSWE t10 [mm]		ΔSWE t11 [mm]		ΔSWE [mm]
Site	HH	VV	HH	VV	HH	VV	HH	VV	in situ
OB	0.819	0.853	0.821	0.841	12.3	12.7	15.4	16.0	14.8
MB	0.670	0.664	0.667	0.668	11.5	11.5	16.1	17.0	12.6
UB	0.596	0.614	0.440	0.508	10.1	9.7	12.2	13.9	11.7
Mean	0.695	0.710	0.643	0.672	11.3	11.3	14.6	15.6	13.0

The random phase error for $N_L = 5.1$ is 0.417 rad for $|\gamma| = 0.6$ and 0.316 rad for $|\gamma| = 0.8$. The corresponding uncertainties for ΔSWE in C-band at $\theta_i = 30°$ are: σ_{SWE} =2.12 mm for $|\gamma| = 0.6$ and 1.61 mm for $|\gamma| = 0.8$. We derived the phase of the corner reflectors, used as reference for ΔSWE = 0, from simulated geosynchronous SAR images with full spatial resolution because the low resolution of the simulated HT product is not suitable for this task. For estimating the error of the corner reflector phase we use the maximum absolute deviation of the phase of a single reflector from the mean value, the same procedure as for full resolution InSAR ΔSWE error estimates. The resulting error estimate for the corner reflector phase is: $\delta_{\Phi,CR} = 0.244$. Combining $\sigma_{\phi,ran}$ and $\delta_{\Phi,CR}$ in quadrature results in the following numbers for the ΔSWE error: $\sigma_{SWE} = 2.46$ mm for $|\gamma| = 0.6$ and $\sigma_{SWE} = 2.03$ mm for $|\gamma| = 0.8$.

The average ΔSWE values of the simulated HT data show for the RoIs slightly higher deviations from the in situ measurements than the full resolution InSAR ΔSWE products. For track 10 ΔSWE of SE1 shows an underestimation of 1.7 mm and for track 11 an overestimation of 2.1 mm. The differences of ΔSWE between HH and VV polarizations are small.

5. Discussion

Airborne L-band and C-band polarimetric and interferometric SAR data, acquired during the field campaign, provided the basis for testing and evaluating various approaches for deriving the snow depth and snow mass in Alpine terrain. During the campaign two snowfall events of different intensity occurred that were spanned by SAR acquisitions. This offered the opportunity to examine impacts of fresh snow accumulation on SAR backscatter signals and on the interferometric phase and

https://doi.org/10.5194/egusphere-2026-2104
Preprint. Discussion started: 8 May 2026

coherence, as well as to evaluate the performance of derived snow products. At the SAR flights the snowpack was completely dry, a precondition for deriving SWE and snow depth from radar phase and backscatter intensity. The first snowfall event (SE1) took place on 5 March 2021, providing fresh snow with a mean depth of 13.7 cm. The second snowfall event (SE2) included several occurrences of snowfall between 14 to 18 March amounting to a mean depth of 43.6 cm. The closest flights before and after the second snowfall took place on 9 March and 19 March. The average density of fresh snow of SE1 was 95 kg m^{-3} and of SE2 145 kg m^{-3}, yielding SWE values of 13 mm and 63 mm.

The SAR data were acquired with DLR's airborne radar system F-SAR, operating in C-band (5.3 GHz) and L-band (1.325 GHz) fully polarimetric mode with a range bandwidth of 384 MHz in C-band and 150 MHz in L-band, providing high slant range resolution. The azimuth resolution of the SAR products was also very high so that cells comprising many resolution elements could be used for signature studies and retrievals. SAR repeat images were acquired on seven days along two tracks with headings exactly north-south (track 10) and south-north (track 11). Six corner reflectors (three east-facing, three west-facing) were put up on snow-free ground in support of calibration and as geolocation reference. The interferometric phase of the corner reflectors was used as reference for deducing the snowfall-related phase from the total interferometric phase. In situ snow measurements focussed at three sections of the study area with moderate topography (RoIs). Coherence and phase images show increased noise on steep slopes, very likely due to due to residual topographic phase errors.

5.1 Response of backscatter intensity and co-polarized phase difference to snowfall events

In order to check the response of radar backscatter to the accumulation of fresh snow we analysed time series of co- and cross-polarized backscatter intensity. The C- and L-band co-polarized backscatter coefficients showed little temporal variability and a slight increase during the flight campaign, probably due to gradual growth of scattering elements triggered by temperature gradients in the snowpack. There are consistent differences backscatter intensity between the RoIs in both frequencies which can be attributed to the roughness of the subnivean ground. The flight after the first snowfall event (FL05 on 6 March) shows for the C-band cross-to co-polarized backscatter ratio (CR) an increase of 0.39 dB, 0.96 dB and 0.99 dB for the RoIs that is mainly caused by the rise of the cross-polarized signals. On the next flight, two days later, the CR values dropped to the previous level. The cause of this transient peak in cross-polarized σ° and CR is unclear. The backscatter contribution of a small amount of very fine-grained snow cannot be a main factor, as the C-band scattering efficiency of fresh snow is very small and the fresh snow depths of the three RoIs (15.6 cm, 13.3 cm, 12.3 cm) do not reflect the different ΔCR values of the RoIs.

The data of the second snowfall event show as well a mismatch between the depth of fresh snow and ΔCR. FL08 on the day after SE2 (19 March) shows for the three RoIs C-band ΔCR values of 0.28 dB, 0.48 dB and 0.55 dB whereas the corresponding ΔSD values amount to 43.2 cm, 45.5 cm and 42.1 cm. A possible cause for the increased CR of FL08 could be the scattering contribution of a melt-freeze crust that formed during transient melt-freeze events on days before the snowfall started. The observations of the Wörgetal campaign show that the change of the C-band VH/VV backscatter ratio, proposed as basis for

https://doi.org/10.5194/egusphere-2026-2104
Preprint. Discussion started: 8 May 2026

deriving the snow depth in Alpine terrain (Lievens et al., 2022), is not applicable for retrieving the depth of fresh snow. Changes in snow microstructure and stratigraphy are important elements for the temporal evolution of the VH/VV backscatter ratio, as tower-based C-band polarimetric backscatter measurements (Brangers et al., 2024) and the analysis of satellite-based C-band time series (Hoppinen et al., 2024B) show.

We checked also the information content of the co-polarized phase difference (CPD) in respect to the depth of freshly fallen snow. In fresh, dry snow horizontal structures dominate (Leinss et al., 2016; 2020). The L-band CPD data of the Wörgetal campaign show very little temporal variability and no response in respect to snowfall. Leinss et al. (2014) detected changes of CPD after fresh snowfall in X-band satellite SAR time series and present a distinct relationship between ΔCPD (ϕ_{VV}-ϕ_{HH}) values and the depth of fresh snow. The FSAR C-band CPD values show minor variations between FL01 and FL07 but no particular response to SE1. Between FL07 (9 March) and FL08 (19 March), the period which includes snowfall SE2 (14 to 18 March,) the C-band CPD values of the RoIs increased in track10 by 0.23 rad and in track 11 by 0.25 rad. The mean depth of fresh snow (ΔSD), measured on 19 March, was 44 cm. However, the comparison with in situ point measurements of fresh snow shows that the ΔSD and ΔCPD samples are uncorrelated. On the other hand, ΔCPD shows an increase with the local radar incidence angle which can be modelled by linear regression yielding a coefficient of determination (R^2) of 0.49. This feature can be attributed to two-way propagation of the radar waves through a frozen crust of several cm thickness that formed on days before the snowfall. Melt-freeze events cause the formation of large grains and polycrystals with horizontal orientation (Domine et al., 2009; Kapil et al., 2010). The anisotropy of snow microstructure induces anisotropy of the dielectric permittivity and results in a propagation delay difference between co-polarized waves (Leinss et al., 2016). The incidence angle dependence of the CPD is a consequence of the shape of the scattering phase function and the increasing path length of radar waves propagating through an anisotropic layer.

5.2 SWE retrievals by inversion of the interferometric phase delay

We studied three configurations as basis for retrieving SWE by means of the interferometric phase delay, using (1) full resolution F-SAR data, (2) split-bandwidth interferometry as an approach for reducing constraints of the 2π phase ambiguity, (3) simulated geosynchronous SAR data. A common element of the three configurations was the use of the phase of corner reflectors cleaned of snow (ΔSWE = 0) as reference for obtaining the phase difference caused by changes in SWE. We performed error estimates for the three configurations, accounting for the phase error of the corner reflectors and the random phase error of the snow pixels which depends on coherence and the number of independent samples. The radar frequency has contrary effects in respect to performance of computed ΔSWE. On one hand, low radar frequencies cover a wider range of SWE values within a 2 π phase cycle and are less susceptible to temporal decorrelation (Rott et al., 2004, Ruiz et al., 2022). On the other hand, high radar frequencies offer higher sensitivity of the DInSAR phase in respect to SWE and the sensors usually have higher range bandwidth and azimuth resolution, resulting in a lower random phase error for a given cell size.

https://doi.org/10.5194/egusphere-2026-2104
Preprint. Discussion started: 8 May 2026

Temporal decorrelation increases with snowfall intensity and radar frequency, as the large drop of the C-band coherence for SE2 shows. The average coherence magnitude over the RoIs of full resolution InSAR data spanning SE1 amounts in L-band to 0.942 and in C-band to 0.788, dropping for SE2 in L-band to 0.764 and in C-band to 0.376. The phase sensitivity in respect to SWE is in C-band four times higher than in L-band which implies larger susceptibility to random phase noise for L-band. This is not a critical issue for the full resolution F-SAR data because cells with a large number of resolution elements can be used. In this case the phase errors of the corner reflectors exceed the random phase errors. The differences in coherence between HH and VV polarizations are small. On average over the RoIs the coherence magnitude of VV-polarized full resolution data exceeds that of HH-polarized data in C-band by 5% and in L-band by 2.5%.

With C-band full resolution SAR data we performed retrievals only for SE1 because ΔSWE of SE2 exceeds the 2π phase threshold up to 3-fold. C- and L-band show similar results for retrieved ΔSWE of SE1, with underestimation of 0.4 mm, respectively 2.1 mm, for track 10 and overestimation of 2.8 mm, respectively 1.3 mm for track 11. VV and HH based ΔSWE values agree within 0.4 mm. The differences between in situ and computed ΔSWE values of individual RoIs and tracks range from -2.9 mm to +4.4 mm. The SE2 L-band ΔSWE retrievals of the RoIs show for track 10 an average value of 68.8 mm and for track 11 a value of 61.2 mm. The in situ ΔSWE value is 63.4 mm. The opposite signs of biases of the two tracks are very likely caused by uncertainties of the reflector phase. The RSMD of computed ΔSWE for SE2 versus in situ point measurement is 7.2 mm. These numbers are within the performance requirement for spatially distributed SWE products (IGOS, 2007),

The Delta-k interferometric method, based on split-bandwidth interferometry, is able to provide ΔSWE data of intense snowfall events because of the larger span of the 2π phase cycle. The split-bandwidth frequency separation determines the sensitivity in respect to the interferometric phase (Bamler and Eineder, 2005). For the Wörgetal Delta-k retrievals we obtained a split-bandwidth frequency separation of 284 MHz in C-band and 100 MHz in L-band. This results in the increase of 2π phase ambiguity compared the full resolution data by a factor of 18.7 in C-band and 13.2 in L-band and causes reductions of the phase sensitivity in respect to SWE by the same numbers. In the selected Delta-k configuration the range resolution of the sub-bands is reduced by a factor of 3.8 in C-band compared to full-bandwidth data and in L-band by a factor of 3.0.

For the SWE retrievals we used cells of 10 m x 15 m extent (azimuth x range) which include in C-band in 163 and in L-band 64 resolution elements in the sub-bands. In L-band the coherence of full resolution and Delta-k data differs by less than 1%. The C-band Delta-k coherence shows a larger decline, in particular for SE2. The site with the highest ground surface roughness, UB, shows the largest drop, resulting in mean $|\gamma| = 0.152$. In order to limit impacts of low coherence pixels we exclude cells with $|\gamma| < 0.3$ for SWE retrievals. This reduces the share of valid SE2 cells for Delta-k ΔSWE retrievals in C-band for OB to 64%, for MB to 56% and for UB to 5%. In L-band the share of valid pixels is larger than 95% in any of the RoIs. In C-band the average random phase errors for Delta-k and full resolution interferometric data are similar because we use a larger cell

https://doi.org/10.5194/egusphere-2026-2104
Preprint. Discussion started: 8 May 2026

size for Delta-k. In L-band the $\sigma_{\phi,ran}$ error is higher by a factor of two because of the reduced number of looks. Nevertheless, the error estimates for the corner reflector phase still exceed that of $\sigma_{\phi,ran}$.

The C-band Delta-k SWE retrievals show for SE1 on average an overestimation of 2 mm which is in the same range as the deviations of the C-band full resolution ΔSWE retrievals. For SE2 the discrepancies are larger, showing for C-band OB and UB an underestimation of 13.8 mm, resulting from underestimation of 9.3 mm in track 10 and 18.3 mm in track 11. The L-band Delta-k SWE retrievals of SE2 show on average an overestimate of 5.0 mm, following from an overestimate of 13.9 mm in track 10 and an underestimate of 4.0 mm in track 11. In case of the SE2 Delta-k SWE retrievals of C-band the low coherence and reduced phase sensitivity in respect to SWE are main factors for the error, for L-band the low phase sensitivity is the main factor.

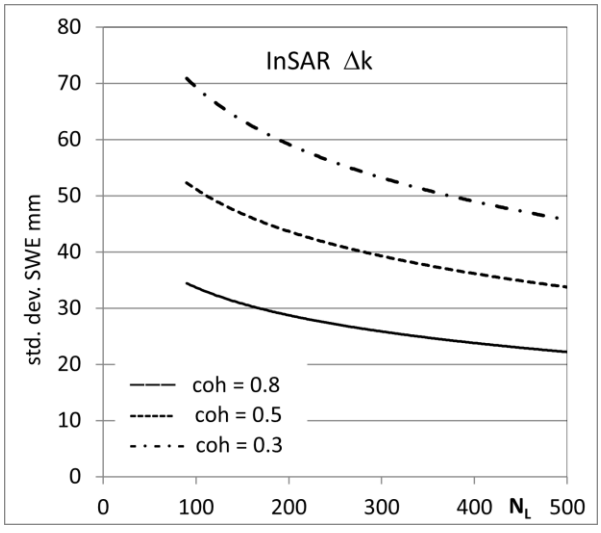

Figure 15: Error (standard deviation) for Delta-k InSAR retrievals in mm water equivalent due to random phase noise in dependence of the number of independent samples, total range bandwidth 100 MHz and split-bandwidth separation 75 MHz, for θ_i = 30° and snow density ρ = 0.3 g cm^{-3}.

In spite of the higher uncertainty of Delta-k InSAR SWE retrievals, the Delta-k approach can fulfil valuable complementary tasks in support of continuous surveys of snow accumulation. A main role of Delta-k can be the detection and correction of errors arising from 2π ambiguities and the bridging of gaps in interferometric SWE times series. Regarding the choice of wavelength, the C- and L-band SWE retrievals show contrary effects regarding coherence and phase sensitivity. For the Delta-k phase sensitivity in respect to SWE the split-bandwidth frequency separation is a critical factor. Figure 15 shows estimates of ΔSWE retrieval errors due to random phase noise for a SAR system with 100 MHz total range bandwidth and 75 MHz split-bandwidth separation by splitting the total bandwidth in two sub-bands of 30 MHz. Such a configuration can be achieved with C- and L-band satellite SAR data. The error estimates show that coherence is decisive for retrieval performance. Deficiencies

https://doi.org/10.5194/egusphere-2026-2104
Preprint. Discussion started: 8 May 2026

can only partly be compensated by increasing the retrieval cell size and number of looks. Considering the larger susceptibility of C-band to decorrelation in case of snowfall, there is a preference for L-band for capturing large snow accumulation.

The study on the feasibility of geosynchronous SAR for SWE monitoring is based on simulated geosynchronous SAR data, exhibiting the same properties as the SAR products of the proposed Earth Explorer 10 mission candidate Hydroterra (ESA, 2020; Hydroterra Mission Team, 2020. The range bandwidth of 6 MHz is much smaller than that of the F-SAR products and also smaller than that of current operational satellite C-band SAR systems. The single look spatial resolution of the simulated HT products is 5 m x 22.2 m (azimuth x range). A specific feature of geosynchronous SAR products is the longer integration time required for SAR image focusing. Integration times up to 110 minutes were applied for deriving HT SAR products from sequences of repeat-pass F-SAR data. During this time span snow physical properties did not change so that the extension of the integration time did not cause degradation of SAR image quality.

The performance of ΔSWE retrievals using simulated HT interferometric products was investigated for SE1. A cell size of 10 x 1 pixels (azimuth x range) was used, corresponding to a surface area of 29.3 m x 38.4 m at $\theta_i = 30$. Due to the low number of independent samples ($N_L = 5.1$) the random phase error exceeds the value of the full resolution F-SAR cells about 10-fold. The corner reflector phase was adopted from simulated geosynchronous SAR data at F-SAR resolution. The effect of the low HT resolution shows up in reduced coherence. As in the case of Delta-k, the site with the highest roughness of the ground surface, UB, shows the largest decrease of coherence. This effect can be attributed to variations of the snow-related phase delay within radar resolution elements over rough surfaces, indicating an impact of surface resolution for the interferometric coherence of snow-covered ground.

The ΔSWE retrievals for SE1 based on HT simulations show similar performance as the retrievals based on full resolution data because the loss of coherence is small. On the other hand, the HT coherence of SE2 is very low, not providing an adequate number of pixels for reliable ΔSWE retrievals. This problem can be overcome by exploiting the dense interferometric repeat coverage capability of geosynchronous SAR. A particular strength of geosynchronous SAR systems is the capability of providing regular repeat observations at short time intervals, mitigating impacts of temporal decorrelation. In order to comprehensively consolidate and assess the capabilities of geosynchronous SAR for SWE retrievals, further issues need to be assessed, including impacts of meteorological conditions on SAR image focusing in dependence of the integration time and constraints in mountain areas imposed by the geosynchronous observation geometry.

6. Conclusion

In March 2021 a field experiment was conducted in the high-Alpine test site Woergetal of the Austrian Alps, collecting interferometric and polarimetric C- and L-band airborne SAR data and performing in situ measurements on snow properties. On seven days airborne flights were undertaken, each of which comprised multiple repeat-pass acquisitions along two tracks with opposite view directions. The flights spanned days without snowfall, as well as two snowfall events of different intensity,

https://doi.org/10.5194/egusphere-2026-2104
Preprint. Discussion started: 8 May 2026

depositing on average 13 mm (SE1) and 63 mm (SE2) of snow water equivalent. Main project objective was the testing and evaluation of procedures for deriving changes in snow mass and snow depth from repeat pass SAR measurements, key parameters for hydrology and water management in Alpine areas. In order to minimize impacts of topography-related noise, the field measurements and the SAR data analysis focused at three central sections (RoIs) in moderately inclined terrain. At the time of the flights the snowpack was completely dry. Throughout the campaign the backscatter intensities showed little temporal change. On a few days between the flights transient melt-freeze events occurred causing the formation of refrozen snow surface crusts.

On the methodological side the focus was on the feasibility and performance of differential radar interferometry (DInSAR) for SWE retrievals, taking into account configurations of current and future spaceborne SAR systems. We studied also the feasibility for deriving the depth of fresh snow from changes of the C-band cross- to co-polarized backscatter intensity and changes of the co-polarized phase difference. None of these two parameters shows a reproducible relationship with the in situ measurements of snow depth or SWE of the two snowfall events. The change of the co-polarized (VV-HH) phase difference of the interferometric time span that covers SE2 and some days before this event shows a pronounced increase of the co-polarized phase difference with the radar incidence angle. This relationship can be attributed to the two-way propagation of the radar signal through a frozen crust that formed on days before the snowfall.

Regarding the DInSAR method for SWE retrieval, we studied the suitability and performance for three different configurations based on the airborne SAR acquisitions: (1) C- and L-band repeat-pass SAR data at full spatial resolution, (2) differential wavenumber (Delta-k) interferograms obtained by split-bandwidth processing of C- and L-band SAR data, (3) simulated geosynchronous C-band SAR data reflecting the properties of the proposed geosynchronous SAR mission Hydroterra (ESA, 2020). We used the phase of the corner reflectors cleaned of snow as reference for deriving the SWE-related phase component from the observed total interferometric phase. Error estimates for computed ΔSWE show that the errors of the reflector phase exceed the random phase errors of the snow pixels. The three configurations, as well as the two frequencies, exhibit differences in spatial resolution, in the susceptibility to phase ambiguities, in the exposure to temporal decorrelation caused by snowfall and in the phase sensitivity in respect to SWE. L-band has lower phase sensitivity than C-band which is, at least partly, compensated by higher coherence. C-band is affected by lower coherence and 2π phase ambiguities, inhibiting the application of configurations (1) and (3) for the intense snowfall case (SE2). The snowfall related decline of coherence is largest in the test field with the highest surface roughness. The comparisons of computed ΔSWE with the in situ measurement data show for configurations (1) and (3) average deviations in the order of a few millimetres water equivalent. The errors are larger for the ΔSWE retrievals by means of Delta-k interferometry because the phase sensitivity largely exceeds that of the two other approaches. On the other hand, due to the larger span of the 2π phase cycle, the Delta-k approach is of interest for detecting and correcting errors arising from 2π phase ambiguities and for bridging gaps in interferometric SWE times series.

https://doi.org/10.5194/egusphere-2026-2104
Preprint. Discussion started: 8 May 2026

Geosynchronous interferometric SAR observations would be able to overcome constraints by temporal decorrelation due to the ability of providing continuous repeat observations with short time spans.

The results of the field experiment confirm the great potential of differential radar interferometry for spatially detailed SWE monitoring. Whereas ambiguities between effects of snow mass and microstructure have to be resolved for deriving SWE from backscatter intensity, the snow microstructure is of minor relevance for the interferometric method using C- and L-band radar frequencies. Critical issues for DInSAR SWE retrievals are the temporal decorrelation and the representativity of the reference phase at points with in situ measurements of SWE or at snow-free sites. Accurate estimates and corrections for the topographic and atmospheric phase terms are also essential. The use of points with interferometric reference phase values is confined to contiguous coherent areas. In order to achieve complete spatial and temporal coverage for SWE monitoring the exploitation of different InSAR data sources will be needed. This study introduces options for complementary use of different radar frequencies and data processing approaches in DInSAR SWE monitoring, providing differences regarding the phase sensitivity to SWE, the susceptibility to temporal decorrelation and the exposure to phase ambiguities. The portfolio of current and future radar satellite missions offers a range of options for the synergistic use of different input data sources and processing approaches. For optimizing the utilization of this potential dedicated feasibility and performance studies for different snow regimes are needed.

Data availability. The field campaign data are accessible at https://earth.esa.int/eogateway/campaigns/sarsimht-ng

Supplement. The supplement related to this article is available online.

Author contributions. Conceptualization: HR, TN, RH, JK, Data Curation, HR, MH, TN, RH, JF, Formal analysis: HR, MH, TN, RH, JF, Investigation: HR, TN, RH, JF, Methodology: HR, MH, TN, RH, Project administration: TN, HR, RH, Software: MH, TN, RH, JF, Supervision: HR, TN, RH, Validation: HR, TN, MH, JK, Writing - original draft: HR. Writing – Review & editing; all authors.

Competing interests. The contact author has declared that none of the authors has any competing interests.

Acknowledgements. Airborne data acquisitions and processing, field measurements and scientific data analysis were performed within the project SARSimHT-NG (Simulation of Hydroterra SAR System Performance in the Mediterranean and the Alps Based on Experimental Airborne SAR Data), supported by the European Space Agency, Contract 4000134680/21/NL/FF/an. Further scientific analysis, with focus on dual frequency approaches, was performed within the project SUPSAR-SNOW, supported by the European Space Agency, Contract No. 4000148102/25/I-EB-bgh.

https://doi.org/10.5194/egusphere-2026-2104
Preprint. Discussion started: 8 May 2026

References

Bamler, R., and Eineder, M.: Split band interferometry versus absolute ranging with wideband SAR systems, in: Proc. IEEE Int. Geosci. Remote Sens. Symp. (IGARSS), Anchorage, Alaska, Sept. 2004, vol. 2, 980–984, 2004.

Bamler, R., and Eineder, M.: Accuracy of differential shift estimation by correlation and split-bandwidth interferometry for wideband and Delta-k SAR systems, IEEE Geosci. Remote Sens. Lett., 2 (2), 151–155, doi: 10.1109/LGRS.2004.843203, 2005.

Bamler, R., and Hartl, P.: Synthetic aperture radar interferometry, Inverse Problems, 14, R1 - R54, 1998.

Bonnell, R., McGrath, D., Tarricone, J., Marshall, H.-P., Bump, E., Duncan, C., Kampf, S., Lou, Y., Olsen-Mikitowicz, A., Sears, M., Williams, K., Zeller, L., and Zheng, Y.: Evaluating L-band InSAR snow water equivalent retrievals with repeat ground-penetrating radar and terrestrial lidar surveys in northern Colorado, The Cryosphere, 18, 3765–3785, https://doi.org/10.5194/tc-18-3765-2024, 2024.

Brangers, I., Marshall, H.-P., De Lannoy, G., Dunmire, D., Mätzler, C., and Lievens, H.: Tower-based C-band radar measurements of an alpine snowpack, The Cryosphere, 18, 3177–3193, https://doi.org/10.5194/tc-18-3177-2024, 2024.

Calonne, N., Geindreau, C., Flin, F., Morin, S., Lesaffre, B., Rolland du Roscoat, S., and Charrier, P.: 3-D image-based numerical computations of snow permeability: links to specific surface area, density, and microstructural anisotropy, The Cryosphere, 6, 939–951, https://doi.org/10.5194/tc-6-939-2012, 2012.

Calonne, N., Flin, F., Geindreau, C., Lesaffre, B., and Rolland du Roscoat, S.: Study of a temperature gradient metamorphism of snow from 3-D images: time evolution of microstructures, physical properties and their associated anisotropy, The Cryosphere, 8, 2255–2274, https://doi.org/10.5194/tc-8-2255-2014, 2014.

Deeb, E. J., Forster, R. R., and Kane, D. L.: Monitoring snowpack evolution using interferometric synthetic aperture radar on the North Slope of Alaska, USA, Int J. Remote Sens., 32 (14), 3985-4003, 2011.

Domine, F., Taillandier, A.-S., Cabanes, A., Douglas, T. A., and Sturm, M.: Three examples where the specific surface area of snow increased over time, The Cryosphere, 3, 31–39, https://doi.org/10.5194/tc-3-31-2009, 2009.

Engen, G., Guneriussen, T., and Overrein, O.: Delta-k interferometric SAR technique for snow water equivalent (SWE) retrieval, IEEE Geosci. Remote Sens. Lett., 1 (2), 57–61, doi: 10.1109/LGRS.2003.822880, 2004.

ESA(2020): Report for Assessment: Earth Explorer 10 Candidate Mission Hydroterra, European Space Agency, Noordwijk, The Netherlands, ESA-EOPSM-HYDRO-RP-3779, 131 p., 2020.

Fierz, C., Armstrong, R.L., Durand, Y., Etchevers, P., Greene, E., McClung, D.M., Nishimura, K., Satyawali, P.K. and Sokratov, S.A.: The International Classification for Seasonal Snow on the Ground, IHP-VII, Technical Documents in Hydrology Nr. 83, IACS Contribution Nr.1, UNESCO-IHP, Paris, 2008.

Gracheva, V., Prats, P., Scheiber, R., Horn, R., Keller, M., Fischer, J., Reigber, A., and Moreira, A.: Simulation of geosynchronous Hydroterra image products with airborne SAR data, Proc. of 13th European Conference on Synthetic Aperture Radar (EUSAR), Leipzig, March 2021, pp. 581-586, 2021.

https://doi.org/10.5194/egusphere-2026-2104
Preprint. Discussion started: 8 May 2026

Guneriussen, T., Hogda, K., Johnsen, H., and Lauknes, I.: InSAR for estimation of changes in snow water equivalent of dry snow, IEEE Trans. Geosci. Remote Sens., 39, 2101–2108, https://doi.org/10.1109/36.957273, 2001.

Hoppinen, Z., Oveisgharan, S., Marshall, H.-P., Mower, R., Elder, K., and Vuyovich, C.: Snow water equivalent retrieval over Idaho – Part 2: Using L-band UAVSAR repeat-pass interferometry, The Cryosphere, 18, 575–592, https://doi.org/10.5194/tc-18-575-2024, 2024A.

Hoppinen, Z., Palomaki, R. T., Brencher, G., Dunmire, D., Gagliano, E., Marziliano, A., Tarricone, J., and Marshall, H.-P.: Evaluating snow depth retrievals from Sentinel-1 volume scattering over NASA SnowEx sites, The Cryosphere, 18, 5407–5430, https://doi.org/10.5194/tc-18-5407-2024, 2024B.

Horn, R., Jaeger, M., Keller, M., Limbach, M., Nottensteiner, A., Pardini, M., Reigber, A., and Scheiber, R.: F-SAR – Recent upgrades and campaign activities, in: Proc. of 13th Int. Radar Symp. (IRS), Prague, Czechia, June 28-30, 2017, pp. 71-77, 2017.

Huang, L., Tian, B., Li, Z., and Zhou, J.: Scattering property analysis of supraglacial debris using target decomposition on polarimetric SAR imagery, IEEE J. Select. Top. Appl. Earth Obs. Rem. Sens.,10 (5), 1843 – 1852, 2017.

Hydroterra Mission Team: Hydroterra Earth Explorer 10 Mission Candidate Mission Assumptions and Preliminary Technical Requirements (MATER), European Space Agency, Noordwijk, The Netherlands Ref: EOP-ΦMP/2018-12-2114, 2020.

Iannini, L., Davidson M. W. J., Osborne, S., Gebert, N., Di Cosimo, G., Mezzasoma, S., Petrolatia, D., Kazimierczak, D., De La Fuente Arranz, C., Miccoli, A., Rojek, A., Nardecchia, L., and Pavia, P.: ROSE-L - The Copernicus Expansion L-Band SAR Mission, in: EUSAR 2024 Proceedings, 15th European Conference on Synthetic Aperture Radar, Munich, Germany, pp. 5-8, 2024.

IGOS: Cryosphere Theme Report, Integrated Global Observing Strategy, WMO/TD-1405, 2007.

Kapil, J. C., Prasher, C., Datt, P., and Satyawali, P. K.: Growth of melt–freeze clusters and formation of impeding layers to water flow in snow irradiated by a sun simulator under controlled laboratory conditions, Ann. Glaciol., 51(54), 19-26, 2010.

Lawinenwarndienst Tirol: Beitrag in Saisonbericht der österreichischen Lawinenwarndienste 2020/21, Herausgeber Arbeitsgemeinschaft österreichischer Lawinenwarndienste, pp. 72-119, 2021.

Lawinen Report: https://lawinen.report/blog/at-07-de/107, https://lawinen.report/blog/at-07-de/108, https://lawinen.report/blog/ at-07-de/109, 2021. (last access: 4 February 2026)

Lei, Y., Siqueira, P., and Treuhaft, R.: A dense medium electromagnetic scattering model for the InSAR correlation of snow. Radio Sci. 51, 461e480, https://doi.org/10.1002/2015RS005926, 2016.

Leinss, S., Parrella, G., Hajnsek, I.: Snow height determination by polarimetric phase differences in X-Band SAR data, IEEE J. Select. Top. Appl. Earth Obs. Rem. Sens., 7, 3794–3810, https://doi.org/10.1109/JSTARS.2014.2323199, 2014.

Leinss, S., Wiesmann, A., Lemmetyinen, J., and Hajnsek, I.: Snow water equivalent of dry snow measured by differential interferometry, IEEE J. Select. Top. Appl. Earth Obs. Rem. Sens., 8, 3773–3790, https://doi.org/10.1109/JSTARS.2015.2432031, 2015.

https://doi.org/10.5194/egusphere-2026-2104
Preprint. Discussion started: 8 May 2026

Leinss, S., Löwe, H., Proksch, M., Lemmetyinen, J., Wiesmann, A., and Hajnsek, I.: Anisotropy of seasonal snow measured by polarimetric phase differences in radar time series, The Cryosphere, 10, 1771–1797, https://doi.org/10.5194/tc-10-1771-2016, 2016.

Leinss, S., Löwe, H., Proksch, M., and Kontu, A.: Modeling the evolution of the structural anisotropy of snow, The Cryosphere, 14, 51–75, https://doi.org/10.5194/tc-14-51-2020, 2020.

Lievens, H., Brangers, I., Marshall, H.-P., Jonas, T., Olefs, M., and De Lannoy, G.: Sentinel-1 snow depth retrieval at sub-kilometer resolution over the European Alps, The Cryosphere 16 (1), 159–177.http://dx.doi.org/10.5194/tc-16-159-2022, 2022.

Mortimer, C., Mudryk, L., Derksen, C., Luojus, K., Brown, R., Kelly, R., and Tedesco, M.: Evaluation of long-term Northern Hemisphere snow water equivalent products, The Cryosphere, 14, 1579–1594, https://doi.org/10.5194/tc-14-1579-2020, 2020.

Oh, Y., Sarabandi, K., and Ulaby, F.T.: Semi-empirical model of the ensemble-averaged differential Mueller Matrix for microwave backscattering from bare soil surface, IEEE Trans. Geosci. Remote Sens., 40 (6), 1348 -1355, 2002.

Orthofotos-Tirol: https://www.tirol.gv.at/sicherheit/geoinformation/geodaten-tiris/orthofotos/, (last access: 04 February 2026), 2020.

Pan, J., Durand, M., Lemmetyinen, J., Liu, D., and Shi, J.: Snow water equivalent retrieved from X- and dual Ku-band scatterometer measurements at Sodankylä using the Markov Chain Monte Carlo method, The Cryosphere, 18, 1561–1578, https://doi.org/10.5194/tc-18-1561-2024, 2024.

Rosen, P. A., Hensley, S., Joughin, I. R., Li, F. K., Madsen, S.N., Rodriguez, E., and Goldstein, R. M.: Synthetic aperture radar interferometry, Proc. IEEE, 88 (3), 333–382, 2000.

Rott, H., Nagler, T., and Scheiber, R.: Snow mass retrieval by means of SAR interferometry, Proc. of ESA Fringe 2003 Workshop, Frascati, Italy, 1-5 Dec. 2003, ESA SP-550, European Space Agency, Noordwijk, The Netherlands, 2004.

Rott, H., Yueh, S. H., Cline, D. W., Duguay, C., Essery, R., Haas, C., Hélière, F., Kern, M., Macelloni, G., Malnes, E., Nagler, T., Pulliainen, J., Rebhan, H., and Thompson, A.: Cold Regions Hydrology High-Resolution Observatory for snow and cold land processes, Proc. IEEE, 98, 752–765, https://doi.org/10.1109/JPROC.2009.2038947, 2010.

Ruiz, J. J., Lemmetyinen, J., Kontu, A., Tarvainen, R., Pulliainen, J., and Praks, J.: Investigation of environmental effects on coherence loss in SAR interferometry for snow water equivalent retrieval, IEEE Trans. Geosci. Remote Sens., 60, 4306714, doi: 10.1109/TGRS.2022.3223760, 2022.

Sarabandi, K.: Derivation of phase statistics from the Mueller matrix, Radio Sci., 27 (5), 553–560, 1992.

Singh, S., Durand, M., Kim, E., and Barros, A. P.: Bayesian physical–statistical retrieval of snow water equivalent and snow depth from X- and Ku-band synthetic aperture radar – demonstration using airborne SnowSAR in SnowEx'17, The Cryosphere, 18, 747–773, https://doi.org/10.5194/tc-18-747-2024, 2024.

https://doi.org/10.5194/egusphere-2026-2104
Preprint. Discussion started: 8 May 2026

Tarricone, J., Webb, R. W., Marshall, H.-P., Nolin, A. W., and Meyer, F. J.: Estimating snow accumulation and ablation with L-band interferometric synthetic aperture radar (InSAR), The Cryosphere, 17, 1997–2019, https://doi.org/10.5194/tc-17-1997-2023, 2023.

Torres, R., Geudtner, D., Davidson M.W.J., Bibby, D., Navas-Traver, I., and Garcia Hernandez, A.I.: Sentinel-1 Next Generation: enhanced C-band data continuity, in: Proc. of 15th European Conference on Synthetic Aperture Radar (EUSAR), Munich, Germany, March 20204, pp. 1-4, 2024.

Tsang, L., Ding, K. H., Huang, S., and Xu, X: Electromagnetic computation in scattering of electromagnetic waves by random rough surface and dense media in microwave remote sensing of land surfaces, Proc. IEEE, 101, 255–279, 2013.

Tsang, L., Durand, M., Derksen, C., Barros, A. P., Kang, D.-H., Lievens, H., Marshall, H.-P., Zhu, J., Johnson, J., King, J., Lemmetyinen, J., Sandells, M., Rutter, N., Siqueira, P., Nolin, A., Osmanoglu, B., Vuyovich, C., Kim, E., Taylor, D., Merkouriadi, I., Brucker, L., Navari, M., Dumont, M., Kelly, R., Kim, R. S., Liao, T.-H., Borah, F., and Xu, X.: Review article: Global monitoring of snow water equivalent using high frequency radar remote sensing, The Cryosphere, 16, 3531–3573, https://doi.org/10.5194/tc-16-3531-2022, 2022.

Ulaby, F. T., and Long, D.G.: Microwave Radar and Radiometric Remote Sensing, University of Michigan Press, Ann Arbor, MI, USA, 2014.

Wiesmann, A., and Mätzler, C.: Microwave emission model of layered snowpacks, Rem. Sens. Env., 70 (3), 307–316, 1999.

Zhu, J., Tan, S., King, J., Derksen, C., Lemmetyinen, J., and Tsang, L.: Forward and inverse radar modeling of terrestrial snow using SnowSAR data, IEEE Trans. Geosci. Remote Sens., 56, 7122–7132, https://doi.org/10.1109/TGRS.2018.2848642, 2018.